International Journal of Hydrogen Energy 135 (2025) 440–456

Contents lists available at ScienceDirect

International Journal of Hydrogen Energy

journal homepage: www.elsevier.com/locate/he

Structural, elastic, optic, electronic, phonon, thermodynamic, and hydrogen storage properties of bialkali alanates M_2LiAlH_6 (M = Na, K)

Çağatay Yamçıçıer [a], Cihan Kürkçü [b,*]

[a] Department of Electricity and Energy, Osmaniye Korkut Ata University, Osmaniye, Türkiye
[b] Department of Electronics and Automation, Kırşehir Ahi Evran University, Kırşehir, Türkiye

ARTICLE INFO

Handling Editor: Dr M Mahdi Najafpour

Keywords:
Hydrogen storage
Electronic properties
Elastic properties
Optical properties
Phonon and thermal properties

ABSTRACT

In this study, the structural, elastic, optical, electronic, phonon, thermodynamic, and hydrogen storage properties of bialkali alanates M_2LiAlH_6 (M = Na, K) were systematically investigated using density functional theory (DFT). The compounds crystallize in a cubic structure and exhibit mechanical and thermodynamic stability, as evidenced by their negative formation enthalpies and positive cohesive energies. Elastic constant calculations revealed that both materials are mechanically stable yet brittle. Optical analyses indicated strong absorption and reflectivity in the ultraviolet region, while electronic band structure results showed that the materials are wide-bandgap semiconductors with direct transitions. Phonon dispersion confirmed the dynamic stability of K_2LiAlH_6, while Na_2LiAlH_6 exhibited imaginary frequencies indicating instability. Thermodynamic properties, including Debye temperature, melting point, and minimum thermal conductivity, support the suitability of these compounds for thermal applications. Furthermore, Na_2LiAlH_6 demonstrated a higher hydrogen storage capacity, both gravimetric (3.42 wt%) and volumetric (100.63 gH_2L^{-1}), meeting the U.S. Department of Energy's volumetric target for 2025.

1. Introduction

The energy crisis and environmental pollution are two interlinked challenges that define the global agenda in the 21st century. The rapid depletion of fossil fuel reserves and their adverse environmental impacts, including greenhouse gas emissions and air pollution, have necessitated the exploration of sustainable and clean energy alternatives. Hydrogen energy has emerged as a promising solution due to its high energy density, versatility, and zero-emission characteristics. However, the efficient storage of hydrogen remains a critical factor in unlocking its full potential. Storing hydrogen energy is essential for addressing the intermittency of renewable energy sources, such as solar and wind, by enabling long-term and large-scale energy storage. Unlike conventional batteries, hydrogen storage offers scalability and flexibility, making it suitable for diverse applications ranging from power generation to transportation. Furthermore, it provides a pathway for decarbonizing hard-to-abate sectors while contributing to global efforts to mitigate climate change [1–3].

The compounds Na_2LiAlH_6 and K_2LiAlH_6 hold significant importance in hydrogen storage. These compounds belong to the class of complex alanates, known for their high hydrogen storage capacities and favorable thermodynamic properties. They play a critical role in advancing the hydrogen economy, particularly by offering energy-dense storage solutions. Their significance lies in their chemical structures, which enable the release of substantial amounts of hydrogen through thermal decomposition or catalyzed reactions. Moreover, their reversible nature, which allows hydrogen to be repeatedly stored and released, provides a major advantage for practical hydrogen storage systems. Their thermal stability ensures safe storage and controlled hydrogen release. In addition, their performance can be further enhanced through catalytic improvements, broadening their potential applications.

Na_2LiAlH_6 and K_2LiAlH_6 also offer significant environmental benefits. Their use reduces dependency on fossil fuels and provides a clean and sustainable energy alternative. Furthermore, their composition from relatively abundant elements minimizes environmental impact during production and usage [4,5].

Na_2LiAlH_6 and K_2LiAlH_6 compounds have been significant research subjects as hydrogen storage materials. Below is a summary of prior studies on the structural, thermodynamic, and mechanical properties of these compounds, along with references:

The perovskite-like crystal structure of Na_2LiAlH_6 was first investigated by Brinks et al. [6] through powder neutron and X-ray diffraction

* Corresponding author.
E-mail address: ckurkcu@ahievran.edu.tr (C. Kürkçü).

https://doi.org/10.1016/j.ijhydene.2025.04.445
Received 14 February 2025; Received in revised form 17 April 2025; Accepted 26 April 2025
Available online 8 May 2025

measurements. These studies confirmed that the compound exhibits an elpasolite-type structure. Wang et al. [7] examined the mechanisms affecting the hydrogen storage performance of Na_2LiAlH_6. They demonstrated that reducing particle size or adding a catalyst could improve its dehydrogenation performance. Graetz et al. [8] investigated the thermodynamic properties of this compound, reporting that the enthalpy and temperature of decomposition increase with the size of alkali metal ions. The structure of K_2LiAlH_6 has also been shown to exhibit a perovskite-type arrangement similar to Na_2LiAlH_6. However, due to the larger ionic size of potassium, differences in structural parameters were observed. K_2LiAlH_6 was found to have a higher decomposition enthalpy than Na_2LiAlH_6, indicating differences in hydrogen storage performance.

The investigation of mechanical, electronic, and thermodynamic properties of transition-metal intermetallics via first-principles calculations provides critical insights into their structural stability and functional applications. In particular, detailed studies on Al–Ti–N systems such as $AlTi_3N$, $AlTi_2N$, $AlTi_4N_3$, and $Al_2Ti_3N_2$ have yielded valuable data on their elastic anisotropies, hardness, and dynamic stability [9]. Similarly, research on the intermetallics and its derivatives has advanced materials engineering by elucidating mechanical strength and electronic structure [10,11]. These works not only demonstrate the predictive power of DFT-based computations for material properties but also guide the design of next-generation functional materials.

When compared with other complex hydrides studied for hydrogen storage, such as $NaAlH_4$ [12], $LiAlH_4$ [13], and Mg_2NiH_4 [14], the bialkali alanates M_2LiAlH_6 (M = Na, K) exhibit competitive or superior performance, particularly in terms of volumetric hydrogen capacity and thermodynamic stability. For instance, $NaAlH_4$ has a gravimetric capacity of ~5.6 wt% but requires higher desorption temperatures and often needs catalyst doping for reversibility. Similarly, Mg_2NiH_4 exhibits moderate hydrogen capacity (~3.6 wt%) but suffers from sluggish kinetics and high operating temperatures. In contrast, Na_2LiAlH_6 offers a balance between storage capacity (3.42 wt%, 100.63 gH_2/L), moderate desorption temperature (256.88 K), and intrinsic thermodynamic stability without requiring dopants. Moreover, unlike $LiAlH_4$, which decomposes exothermically and irreversibly under moderate temperatures, M_2LiAlH_6 compounds maintain structural and mechanical integrity. These comparisons suggest that bialkali alanates not only meet but in some cases exceed the performance metrics of traditional alanates and intermetallic hydrides, positioning them as promising candidates for next-generation solid-state hydrogen storage systems.

This study presents an in-depth and multifaceted first-principles investigation of the bialkali alanates Na_2LiAlH_6 and K_2LiAlH_6, aiming to fill critical knowledge gaps in their characterization for hydrogen storage applications. While previous literature has largely focused on isolated properties, such as crystal structure or decomposition thermodynamics, our work offers a holistic approach by simultaneously examining their structural, elastic, optical, electronic, phonon, thermodynamic, and hydrogen storage properties using state-of-the-art density functional theory (DFT) methods. For the first time, we report a complete set of elastic constants, anisotropy indices, mechanical hardness estimations, and phonon dispersion curves for these compounds, enabling a thorough evaluation of their mechanical and dynamic stability. Our findings reveal that Na_2LiAlH_6 not only meets but significantly surpasses the U.S. Department of Energy's volumetric hydrogen storage target for 2025, with a capacity of 100.63 gH_2/L, making it a strong candidate for practical applications. Moreover, the optical properties suggest high UV reflectivity and absorption, opening potential avenues in optoelectronic technologies. The observation of dynamic stability in K_2LiAlH_6, contrasted by the instability in Na_2LiAlH_6, provides critical insight into composition-dependent vibrational behavior. By integrating all these perspectives, this study not only advances the fundamental understanding of complex alanates but also identifies viable pathways for next-generation solid-state hydrogen storage materials.

2. Computational details

The Siesta Package Program [15] was utilized to analyze various physical properties of M_2LiAlH_6 (M = Na, K) compounds, including structural, electronic, elastic, vibrational, optical, and hydrogen storage properties. This research was based on Density Functional Theory (DFT) principles, applying the Perdew-Burke-Ernzerhof (PBE) [16] function within the Generalized Gradient Approximation (GGA) and the Ceperley-Alder (CA) [17] function within the Local Density Approximation (LDA) [18] to handle exchange-correlation energy. Before initiating calculations, geometry optimizations were conducted, selecting the most stable and lowest-energy configurations for simulation. Norm-conserving pseudopotentials of the Troullier-Martins type were employed for Na, K, Li, Al, and H atoms [19], and a double zeta polarized basis set was used throughout. Following optimization, the mesh cut-off energy was set at 300 Ry. For Brillouin zone sampling, a k-point mesh was applied using the Monkhorst-Pack method [20], with meshes defined as 6x6x6 for M_2LiAlH_6. Structural refinement continued through the conjugate-gradient (CG) method until residual forces on all atoms were less than 0.01 eV/Å^{-1}. The Vesta program [21] further aided by providing detailed information on each compound's space group, lattice parameters, and atomic positions. Finally, the volume-conserving method along with the Siesta program was employed to determine the second-order independent elastic constants for M_2LiAlH_6. The cubic crystal system has the simplest form of elastic matrix, with only three independent constants, $C11$, $C12$, and $C44$ [22]:

$$C_{Cubic} = \begin{bmatrix} C_{11} & C_{12} & C_{12} & & & \\ . & C_{11} & C_{12} & & C_{44} & \\ . & . & C_{11} & & & \\ & & & C_{44} & & \\ & & & & C_{44} & \\ & & & & & C_{44} \end{bmatrix}$$

Besides, some elastic constants such as Bulk modulus using $B_H = \frac{B_V+B_R}{2}$, Shear modulus using $G_H = \frac{G_V+G_R}{2}$, Young's modulus using $E = \frac{9GB}{(3B+G)}$ and Poisson's ratio using $\nu = \frac{(3B-2G)}{2(3B+G)}$ were also calculated from the calculated elastic constant values.

3. Results and discussion

3.1. Structural properties

The structure of bialkali alanates, M_2LiAlH_6 (M = Na, K), is seen in Fig. 1. This quaternary phase crystallizes in the cubic system with space group $Fm\bar{3}m$ (225). The unit cell of M_2LiAlH_6 (M = Na, K) compounds comprises 40 atoms: 8 M atoms (Na or K), 4 Li atoms, 4 Al atoms, and 24H atoms. In the compound Na_2LiAlH_6, the positions of the atoms are as follows: Na occupies the 8c position (0.2500, 0.7500, 0.2500), Li is located at the 4b position (0, 0, 0.5000), Al is found at the 4a position (0, 0, 0), and H is situated at the 24e position (0, 0, 0.7613). In the compound K_2LiAlH_6, the positions of the K, Li, Al, and H atoms are as follows: K occupies the 8c position at (0.2500, 0.2500, 0.7500), Li is located at the 4b position (0.5000, 0, 0), Al is found at the 4a position (0, 0, 0), and H is situated at the 24e position (0.2286, 0, 0). All structures were optimized under conditions of zero temperature and pressure. The results are presented in Table 1, which includes lattice parameter, unit cell volume, formation energy, and cohesive energy, compared with other studies in the literature. The results presented in Table 1 align with previous theoretical and experimental studies reported in the literature [6,23–25]. The optimized structure for Na_2LiAlH_6 (GGA-LDA) displays average bond lengths of Al–H (1.75–1.74 Å), Li–H (1.92–1.84 Å), Na–H (2.60–2.53 Å), Li–Al (3.67–3.58 Å), and Li–Na (3.18–3.10 Å). The optimized average bond lengths for K_2LiAlH_6 (GGA -LDA) are as follows: Al–H (1.79–1.77 Å), Li–H (2.12–2.02 Å), K–H (2.77–2.68 Å), Li–Al (3.91–3.79 Å), and Li–K (3.39–3.28 Å).

The thermal stability of alanates is a key factor influencing their effectiveness in solid-state hydrogen storage, as it directly affects the

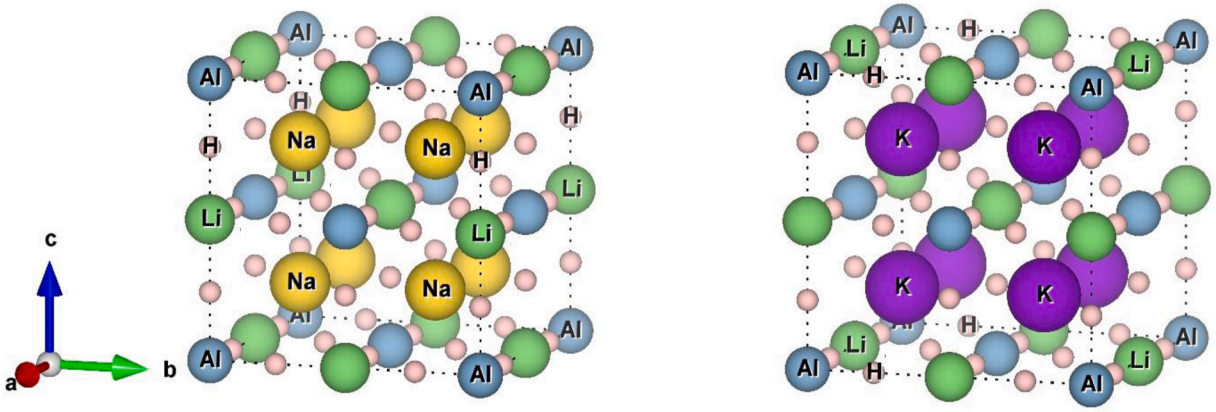

Fig. 1. Crystal structures for M_2LiAlH_6 (M = Na, K).

Table 1
Lattice parameters (a, b, c), volume (V), formation energy (ΔH_f) and cohesive energy (E_{coh}) for **Na_2LiAlH_6,** and K_2LiAlH_6 using both GGA and LDA.

Compound	a (Å)	b (Å)	c (Å)	V (Å^3)	ΔH_f (eV/atom)	E_{coh} (eV/atom)	References
Na_2LiAlH_6 (GGA)	7.3429	7.3429	7.3429	395.92	−0.348	3.127	This study
Na_2LiAlH_6 (LDA)	7.1552	7.1552	7.1552	366.32	−0.437	3.117	This study
	7.3848	7.3848	7.3848	–	–	–	[6]
	7.3380	7.3380	7.3380	–	–	–	[23]
	7.4065	7.4065	7.4065	–	–	–	[24]
K_2LiAlH_6 (GGA)	7.8265	7.8265	7.8265	479.41	−0.381	3.097	This study
K_2LiAlH_6 (LDA)	7.5771	7.5771	7.5771	435.03	−0.516	3.336	This study
	7.9383	7.9383	7.9383	–	–	–	[25]

amount and duration of hydrogen retention. To evaluate the thermal stability of M_2LiAlH_6 (M = Na, K) alanates, we performed measurements to ascertain their enthalpy of formation (ΔH_f). The formation energy was determined using the equation presented in Equation (1) [26].

$$\Delta H_f = E_{tot}(M_2LiAlH_6) - 2E_{tot}(MH) - E_{tot}(LiH) - E_{tot}(Al) - \frac{3}{2}E_{tot}(H_2) \quad (1)$$

In Equation (1), $E_{tot}(M_2LiAlH_6)$, $E_{tot}(MH)$, $E_{tot}(LiH)$, $E_{tot}(Al)$, and $E_{tot}(H_2)$ denote the total energies of MH (Na, K), LİH, Al and H_2, respectively. The formation enthalpies calculated for Na_2LiAlH_6, and K_2LiAlH_6 are −0.348 (GGA), −0.437 (LDA), −0.381 (GGA), and −0.516 (LDA) eV/atom, respectively. A negative formation energy value signifies thermodynamic stability and the feasibility of experimental synthesis [27,28]. K_2LiAlH_6 exhibits enhanced stability due to its more negative formation enthalpy energy. The cohesive energy, represented as E_{coh}, serves as a critical parameter for evaluating system stability. Bond strength denotes the energy necessary to disrupt atomic bonds in a crystal and isolate its individual components. The magnitude of E_{coh} indicates the stability of the crystal. Equation (2) delineates the formula for the cohesive energy of the M_2LiAlH_6 (M = Na, K) compound [29].

$$E_{coh} = -\frac{1}{10}\left[E_{tot}(M_2LiAlH_6) - 2E_{tot}(MH) - E_{tot}(LiH) - E_{tot}(Al) - \frac{3}{2}E_{tot}(H_2)\right] \quad (2)$$

The term $E_{tot}(M_2LiAlH_6)$ denotes the total energy of the M_2LiAlH_6 compound, while $E_{tot}(MH)$, $E_{tot}(LiH)$, $E_{tot}(Al)$, and $E_{tot}(H_2)$ represent the energy of each individual atom within the unit cell. Table 1 illustrates that the heat release observed during the process is positive, signifying a transition from isolated atoms to chemical compounds [30]. The findings indicate the thermodynamic stability of all examined materials.

3.2. Mechanical properties

3.2.1. The elastic constant

The elastic parameters of the bialkali alanates Na_2LiAlH_6 and K_2LiAlH_6 are yet not reported in previous literature to the best of our extensive survey. The elastic properties of a solid are primarily influenced by interatomic interactions and are also beneficial for comprehending a variety of solid-state properties at equilibrium, including bonding nature, structural stability, elastic response to external stress, and machinability. Three independent elastic constants: C_{11}, C_{12}, and C_{44}, are present in a material with cubic symmetry. A cubic system is said to be mechanically stable if it justifies the following elastic stability conditions [31]. Due to the crystal symmetry of a cubic structure, C_{11}═C_{22} = C_{33}, C_{12}═C_{23} = C_{13} and C_{44}═C_{55} = C_{66}. The elastic constants calculated for bialkali alanates Na_2LiAlH_6 and K_2LiAlH_6 compounds are shown in Table 2. According to Born-Huang conditions, a cubic system needs to meet the following requirements in order to be mechanically stable [31]: $C_{11} - C_{12} > 0$; $C_{11} + 2C_{12} > 0$; $C_{44} > 0$. All elastic constants of M_2LiAlH_6 (M = Na, K) compounds meet the criterion for mechanical stability. Consequently, this suggests that M_2LiAlH_6 (M = Na, K) compounds exhibit mechanical stability.

The diagonal elastic constants C_{11}, C_{22}, and C_{33} indicate a material's ability to endure tensile stress in the crystallographic a-, b-, and c-directions, respectively. In cubic crystals, the equality C_{11}═C_{22} = C_{33} indicates that the binding forces along the crystallographic directions a- b- and c-are uniform for M_2LiAlH_6 (M = Na, K) compounds. The diagonal elastic constants, C_{44}, C_{55}, and C_{66}, are used to assess a material's reaction to shearing stress. C_{44} estimates the resistance to shear resulting from tangentially applied stress on the (100) plane in the [010] direction. At the same time, C_{44} represents the indentation hardness of a material. The lower value of C_{44} relative to C_{11} in M_2LiAlH_6 (M = Na, K) compounds indicates that the crystal exhibits lowered resistance to shearing strain. It is anticipated that the mechanical failure mode of M_2LiAlH_6 (M = Na, K) will be affected by shearing strain, as opposed to unidirectional strains. The off-diagonal shear components, specifically

Table 2
Computed elastic constants (C_{ij}), Cauchy pressure (C_p), tetragonal shear constant (C') and Kleinman parameter (ζ) for **Na_2LiAlH_6,** and K_2LiAlH_6 using both GGA and LDA.

Compounds	C_{11}(GPa)	C_{12}(GPa)	C_{44}(GPa)	$C_P(C_{12}–C_{44})$(GPa)	C' (GPa)	ζ	Reference
Na_2LiAlH_6 (GGA)	65.84	20.51	32.40	−11.89	22.67	0.46	This study
	64.76	20.30	31.94	−11.64	22.23	–	[36]
Na_2LiAlH_6 (LDA)	80.12	21.97	34.99	−13.02	29.08	0.42	This study
	78.79	21.82	34.44	−12.62	22.23	–	[36]
K_2LiAlH_6 (GGA)	48.82	21.04	35.01	−13.97	13.89	0.57	This study
	47.86	20.78	34.58	−13.80	13.54	–	[36]
K_2LiAlH_6 (LDA)	69.04	26.28	42.42	−16.14	21.38	0.52	This study
	65.62	22.81	39.99	−17.18	21.40	–	[36]

C_{12}, C_{13}, and C_{23}, indicate a crystal's resistance to volume-conserving orthogonal distortions. The lower value of C_{12} compared to C_{11} in M_2LiAlH_6 (M = Na, K) indicates that the material has less resistance to orthogonal distortions.

One important measurement for determining the dynamical stability of a crystalline solid is the tetragonal shear modulus, C', which is defined as $C' = \frac{C_{11}-C_{12}}{2}$ [32,33]. It also provides insight on the rigidity of a crystal. Moreover, C' is associated with slow transverse acoustic waves and is integral to the structural alterations of a system [34]. The stability of a crystalline compound can be measured by a positive value of C', while a negative value of C' implies that the material is dynamically unstable. The C' values obtained for M_2LiAlH_6 (M = Na, K) are presented in Table II. The positive values of C' values for the calculated compounds indicate the dynamic stability of these compounds. The Kleinman parameter, ζ, which quantifies a compound's stability under bending and stretching, has also been calculated. The Kleinman parameter ($\zeta = \frac{C_{11}+8C_{12}}{7C_{11}+2C_{12}}$) is a dimensionless quantity that typically ranges from 0 to 1. The Kleinman parameter [35] qualitatively indicates the contributions of bond bending and bond stretching to the material's mechanical strength. The Kleinman parameter states that the lower limit of ζ represents a significant contribution of bond stretching or shrinkage in resisting external stress, while the upper limit reflects a significant contribution of bond bending in resisting external load. Table 2 shows that the Kleinman parameter values for Na_2LiAlH_6 compound are 0.46 (GGA), 0.42 (LDA) and for K_2LiAlH_6 0.57 (GGA), 0.52 (LDA). According to the calculated Kleinman parameter values, for Na_2LiAlH_6 compound, both bond bending and bond stress contributions play a role in determining its mechanical strength, while for K_2LiAlH_6 compound, the Kleinman parameter value is greater than 0.5, which means that the mechanical strength is mainly provided by bond bending contributions.

We have additionally computed the Cauchy pressure, C_P, which represents the $C_p = C_{12} - C_{44}$ characteristics of bonding in a structure at the atomic scale [37,38]. A material exhibiting positive Cauchy pressure is generally classified as ductile, whereas brittleness is indicated by a negative value. According to Pettifor [39], materials with a large positive value of C_P exhibit strong metallic non-directional bonding, whereas a negative value of C_P is associated with an angular character in the bonding. Cauchy pressure as calculated for M_2LiAlH_6 (M = Na, K) is presented in Table II. The negative value of C_P for M_2LiAlH_6 (M = Na, K) suggests the brittle nature of M_2LiAlH_6 (M = Na, K) as well as the existence of angular character bonding in the compounds.

3.2.2. The elastic moduli

Elastic moduli for polycrystalline materials can be derived from the elastic constants of single crystals [40]. Table 3 presents the computed polycrystalline bulk modulus (B_H), shear modulus (G_H), Pugh's ratio (B/G), Young's modulus (E), Poisson's ratio (υ), and machinability index (μ^M) for Na_2LiAlH_6 and K_2LiAlH_6. The bulk and shear moduli of polycrystalline materials are calculated applying the Voigt and Reuss approximations [41,42]. These methods provide the mathematical upper and lower bounds of the elastic moduli. The Hill approximation [43] utilizes the arithmetic mean of these two limits and accurately indicates the true polycrystalline constants.

The bulk modulus, $\left(B_H = \frac{B_V+B_R}{2}\right)$, and the shear modulus, $\left(G_H = \frac{G_V+G_R}{2}\right)$, of a material denote its ability to endure volume alterations induced by isotropic pressure and plastic deformation resulting from shear, respectively. The expected elastic constant calculations reveal that the lower shear modulus compared to the bulk modulus suggests that the applied shear component can govern the mechanical failure of M_2LiAlH_6 (M = Na, K). Pugh's ratio (B/G), which measures a solid's bulk to shear modulus ratio, is used to determine whether a material is brittle or ductile [44–47]. The threshold value of the B/G ratio used to determine the brittleness and ductility of materials is 1.75. Ductility correlates with a Pugh's ratio exceeding 1.75, whereas solids with a ratio below 1.75 demonstrate brittleness [33,48,49]. Consequently, the computed Pugh's ratio for M_2LiAlH_6 (M = Na, K) compounds indicates the material's brittle nature, aligning with the principles of Cauchy pressure. Young's modulus, $\left(E = \frac{9GB}{(3B+G)}\right)$, is defined as the ratio of tensile stress to longitudinal strain, quantifying the stiffness of a material. As can be seen from Table 3, both the bulk modulus and Young's modulus of K_2LiAlH_6 are lower than that of Na_2LiAlH_6. The fact that the Young's modulus of K_2LiAlH_6 compound has a lower value indicates that it has less hardness than Na_2LiAlH_6 compound.

Poisson's ratio, $\left(\nu = \frac{(3B-2G)}{2(3B+G)}\right)$, is a commonly utilized parameter that characterizes many properties, including ductility or brittleness, compressibility, and bonding force characteristics of a material.

Table 3
Polycrystalline bulk moduli B_R, B_V, and B_H, shear moduli G_R, G_V, and G_H, Young's modulus E (all in GPa), Pugh's ratio B/G, Poisson's ratio (υ) and machinability index (μ^M) for **Na_2LiAlH_6,** and K_2LiAlH_6 using both GGA and LDA.

Compounds	B_R	B_V	B_H	G_R	G_V	G_H	E	B/G	υ	μ^M	Reference
Na_2LiAlH_6 (GGA)	35.62	35.62	35.62	27.65	28.50	28.08	66.70	1.27	0.187	1.10	This study
	35.12	35.12	35.12	27.19	28.06	27.63	65.66	1.27	0.19	–	[36]
Na_2LiAlH_6 (LDA)	41.35	41.35	41.35	32.36	32.63	32.49	77.24	1.27	0.189	1.18	This study
	40.81	40.81	40.81	31.78	32.06	31.92	75.96	1.28	0.19	–	[36]
K_2LiAlH_6 (GGA)	30.30	30.30	30.30	21.77	26.56	24.16	57.18	1.25	0.185	0.87	This study
	29.81	29.81	29.81	21.32	26.17	23.74	56.29	1.25	0.18	–	[36]
K_2LiAlH_6 (LDA)	40.53	40.53	40.53	30.44	34.01	32.22	76.42	1.26	0.186	0.96	This study
	37.08	37.08	37.08	29.68	32.56	31.12	72.95	1.19	0.17	–	[36]

Poisson's ratio also indicates a material's resilience under shear stress. Enhanced stability against shear is anticipated if the value of υ is somewhat lower. The value of Poisson's ratio is typically in the range of −0.5 to 1.0. The critical value for determining the brittleness and ductility of Poisson's ratio for crystalline materials is approximately 0.26 [50]. A material is classified as ductile if the value of υ exceeds 0.26, and as brittle if it is less than 0.26. Consequently, the value of υ for M_2LiAlH_6 (M = Na, K), as presented in Table 3, signifies the material's brittle characteristics. Our prediction aligns entirely with the previously examined elastic parameters in our work. Poisson's ratio can be used to determine the nature of chemical bonds in solid crystals. In covalent materials, the value of ν is low (about $\nu \sim 0.10$); for ionic materials, the normal value of ν is around 0.25; and for metallic materials, ν is generally about 0.33 [51]. The Poisson's ratio of M_2LiAlH_6 (M = Na, K) lies between these two specific values, indicating that the chemical bonding in these hydrides is a hybrid of covalent and ionic characteristics. Moreover, Poisson's ratio offers additional understanding of the characteristics of the bonding forces. The observed range of ν for central-force solids is 0.25–0.50. If ν lies within this range, the solid is deemed to possess center inter-atomic forces. Otherwise, it is categorized as a non-central force solid [52,53]. Poisson's ratio values for the M_2LiAlH_6 (M = Na, K) compound are less than 0.25, indicating the presence of non-central forces.

Machinability, defined as the ease with which a material can be machined using cutting or shaping tools, is quantified by a parameter referred to as the machinability index ($\mu^M = \frac{B}{C_{44}}$) [54]. Data concerning the machinability of a material is increasingly significant in contemporary industry, as it delineates the optimal economic parameters for machine utilization, cutting forces, temperature, and plastic deformation. Machinability index can also serve as an indicator of a material's flexibility and lubricating properties [55,56]. Na_2LiAlH_6 exhibits a greater μ^M in comparison to K_2LiAlH_6. The elastic moduli of Na_2LiAlH_6 above those of K_2LiAlH_6, suggesting that Na_2LiAlH_6 is better suited for tool applications compared to K_2LiAlH_6.

3.2.3. Hardness

Hardness is a critical property of a solid in engineering for the design of various devices. The hardness value can be calculated using the elastic moduli. Understanding the resistance of solids to localized plastic deformation is essential for assessing their quality. Understanding the mechanical and structural responses of a material under stress is essential. C_{44} and G are acknowledged as the most dependable indices of solid hardness, reflecting the material's capacity to withstand stress [57,58]. Some equations for Miao [59], Chen [60], Tian [61], Teter [62], and Mazhnik [63] used to calculate the hardness values of materials are shown below.

$$(H_V)_{Miao} = \frac{(1-2\nu)\mathrm{E}}{6(1+\nu)} \tag{3}$$

$$(H_V)_{Chen} = 2\left[\left(\frac{G}{B}\right)^2 G\right]^{0.585} - 3 \tag{4}$$

$$(H_V)_{Tian} = 0.92\left(G/B\right)^{1.137} G^{0.708} \tag{5}$$

$$(H_V)_{Teter} = 0.151G \tag{6}$$

$$(H_V)_{Mazhnik} = \gamma_0 \chi(\sigma) E \tag{7}$$

$\chi(\sigma)$ in Equation (7) is a function of the poison ratio and is calculated as follows:

$$\chi(\sigma) = \frac{1 - 8.5\sigma + 19.5\sigma^2}{1 - 7.5\sigma + 12.2\sigma^2 + 19.6\sigma^3} \tag{8}$$

Also γ_0 is a dimensionless constant a value of 0.096.

The $(H_V)_{miao}$, $(H_V)_{Chen}$, $(H_V)_{Tian}$, $(H_V)_{Teter}$, and $(H_V)_{Mazhnik}$ values obtained for the M_2LiAlH_6 (M = Na, K) compounds are presented in Table 4.

As can be seen from Table 4, the average hardness values for both materials are very close to each other in the calculations performed the LDA method. However, according to the calculations performed GGA method, the average hardness value shows that Na_2LiAlH_6 compound is larger than K_2LiAlH_6.

3.2.4. Elastic anisotropy

Elastic anisotropy describes how the mechanical qualities of a compound change depending on the direction they are pointing. It is important to understand elastic anisotropy when designing materials because it affects factors like lattice distortion, plastic deformation, the formation of micro-cracks, and objects breaking down mechanically. Table 5 shows the elastic anisotropy parameters that were determined. Shear anisotropy factors quantify the extent of anisotropy in atomic bonding across various planes inside a crystal. The shear anisotropy of a cubic crystal can be assessed by three distinct parameters [40,64].

Shear anisotropy factor between ⟨011⟩ and ⟨010⟩ directions for shear plane {100},

$$A_1 = \frac{C_{44}}{(C_{11} + C_{33} - 2C_{13})} \tag{9}$$

Shear anisotropy factor between ⟨101⟩ and ⟨001⟩ directions for shear plane {010},

$$A_2 = \frac{4C_{55}}{C_{22} + C_{33} - 2C_{23}} \tag{10}$$

Shear anisotropy factor between ⟨110⟩ and ⟨010⟩ directions for shear plane {001},

$$A_3 = \frac{4C_{66}}{(C_{11} + C_{22} + -2C_{12})} \tag{11}$$

Materials exhibiting isotropy in the bonding between distinct atomic planes has unit values of A_1, A_2, and A_3 ($A_1 = A_2 = A_3 = 1$), while any deviation from unity indicates anisotropy within the material. The obtained anisotropic factor values are shown in Table 5. It is seen that A_1, A_2, and A_3 values are different from 1. The anisotropy factors indicate that M_2LiAlH_6 (M = Na, K) compounds exhibit moderate anisotropy concerning shearing stress across various crystal planes, with all components of the shear anisotropic factors being equal, signifying cubic symmetry. The atomic orbitals that form bonds in various crystal planes and orientations are the source of this anisotropy. Table 5 shows that the anisotropic behavior of K_2LiAlH_6 is higher than that of Na_2LiAlH_6. The following formula has been used to compute the Zener anisotropy (A) factor [65]:

$$A = \frac{2C_{44}}{C_{11} - C_{12}} \tag{12}$$

The Zener anisotropy factor is equivalent to the shear anisotropy factor of M_2LiAlH_6 (M = Na, K) compounds.

The log-Euclidean (A^L) formula is defined by the following equation [66]:

$$A^L = \sqrt{\left[\ln\left(\frac{B_V}{B_R}\right)\right]^2 + 5\left[\ln\left(\frac{C_{44}^V}{C_{44}^R}\right)\right]^2} \tag{13}$$

The Voigt and Reuss approximations for the elastic constant C_{44} are represented by the constants $C_{44}^V = \frac{3}{5}\frac{(C_{11}-C_{12}-2C_{44})}{3(C_{11}-C_{12})+4C_{44}}$ and $C_{44}^R = \frac{5}{3}\frac{C_{44}(C_{11}-C_{12})}{3(C_{11}-C_{12})+4C_{44}}$, respectively [67].

According to Kube and Jong [66,68], the value of A^L for inorganic crystalline compounds is within the range of 0–10.26, with 90 % of these compounds having A^L values less than 1. $A^L = 0$ in the case of perfect

Table 4
Calculated hardness values (GPa) for **Na_2LiAlH_6,** and K_2LiAlH_6 using both GGA and LDA.

Compound	$(H_V)_{Chen}$	$(H_V)_{Tian}$	$(H_V)_{Teter}$	$(H_V)_{Miao}$	$(H_V)_{Mazhnik}$	$(H_V)_{avg}$
Na_2LiAlH_6 (GGA)	7.65	7.13	4.24	5.84	3.86	5.74
Na_2LiAlH_6 (LDA)	8.56	7.88	4.91	6.74	4.44	6.51
K_2LiAlH_6 (GGA)	6.89	6.52	3.65	5.08	3.39	5.10
K_2LiAlH_6 (LDA)	8.66	7.96	4.87	6.75	4.49	6.54

Table 5
Shear anisotropic factors (A_1, A_2, and A_3), anisotropy in compressibility A_B, anisotropy in shear A_G, the universal anisotropy index A^U and d_E, equivalent Zener anisotropy measure, A^{eq}, universal log-Euclidean index A_L, Bulk modulus (in GPa) B_a, along crystallographic axes a, and the anisotropy of linear bulk moduli (A_{B_a} and A_{B_c}) along a and c axes for **Na_2LiAlH_6,** and K_2LiAlH_6 using both GGA and LDA.

Parameters	Na_2LiAlH_6 (GGA)	Na_2LiAlH_6 (LDA)	K_2LiAlH_6 (GGA)	K_2LiAlH_6 (LDA)
A	1.429	1.203	2.521	1.984
A_1	1.429	1.203	2.521	1.984
A_2	1.429	1.203	2.251	1.984
A_3	1.429	1.203	2.251	1.984
A_B	0.000	0.000	0.000	0.000
A_G	0.015	0.004	0.099	0.055
A^U	0.155	0.041	1.101	0.586
d_E	2.481	2.458	2.665	2.566
A^{eq}	1.429	1.203	2.521	1.984
A^L	0.198	0.055	1.134	0.673
B_a	106.86	124.06	90.90	121.60
$\mathbf{A_{B_a}}$	1.000	1.000	1.000	1.000
$\mathbf{A_{B_c}}$	1.000	1.000	1.000	1.000

isotropy. It is challenging to determine whether a material is stratified or lamellar based on the value of A^L. However, the bulk (78 %) of these inorganic crystalline compounds with a high A^L value have a layered or lamellar structure [66]. Compounds with elevated A^L values have pronounced layered structural characteristics, while those with diminished A^L values display non-layered structures. Based on the relatively low value of A^L, it can be anticipated that K_2LiAlH_6 will display a moderately layered configuration. However, with the extremely low value of A^L, Na_2LiAlH_6 is anticipated to demonstrate a non-layered characteristic and exhibits a minimal degree of anisotropy specifically.

The following universal equations are used to determine the universal anisotropy index, (A^U), equivalent Zener anisotropy measure, A^{eq}, percentage anisotropy in compressibility, A_B, and anisotropy in shear, A_G, for crystals:

$$A^U = \frac{B_V}{B_R} + 5\frac{G_V}{G_R} - 6 \geq 0 \tag{14}$$

$$d_E = \sqrt{A^U + 6} \tag{15}$$

$$A^{eq} = \left(1 + \frac{5}{12}A^U\right) + \sqrt{\left(1 + \frac{5}{12}A^U\right)^2 - 1} \tag{16}$$

$$A_B = \frac{B_V - B_R}{B_V + B_R} \tag{17}$$

$$A_G = \frac{G_V - G_R}{G_V + G_R} \tag{18}$$

The universal anisotropy index, which offers a unique way to quantify bulk anisotropy in solids, was established by Ranganathan and Ostoja Starzewski [69]. A^U is known as universal because it may be applied to a wide range of crystal symmetries. $A^U = 0$ is the prerequisite for an isotropic crystal. The fact that the calculated A^U value has values other than 0 indicates the anisotropy of the M_2LiAlH_6 (M = Na, K) compounds. All values of the Zener anisotropy index (A^{eq}) other than 1 indicate anisotropy. The A^{eq} value calculated for the (M = Na, K) compounds shows from Table 5 that these compounds are moderately anisotropic. For A_B and A_G, a value of zero indicates elastic isotropy, whereas a value of one signifies the utmost anisotropy. Chung and Buessem [70] chose not to extend A_G to crystals with lesser symmetries due to the effect of the bulk modulus, alongside the shear modulus, on the anisotropy of non-cubic symmetric crystal [70]. A_G significantly predicts a lower anisotropy index compared to other measurements. A_B zero value of A_B, representing the percentage of anisotropy in compressibility, for M_2LiAlH_6 (M = Na, K) compounds with a cubic structure indicates that the bulk modulus does not affect the anisotropic elastic and mechanical characteristics.

The anisotropies of the bulk modulus and bulk modulus along the a-, b-, c-axis, also known as the directional bulk modulus or bulk modulus under uniaxial strain, are defined as follows [40]:

$$B_a = a\frac{dP}{da} = \frac{\mathrm{D}}{1+\alpha+\beta}, B_b = b\frac{dP}{db} = \frac{B_a}{\alpha}, B_c = c\frac{dP}{dc} = \frac{B_a}{\beta} \tag{19}$$

Where $\mathrm{D} = C_{11} + 2C_{12}\alpha + C_{22}\alpha^2 + 2C_{13}\beta + C_{33}\beta^2 + 2C_{23}\alpha\beta$ and for cubic crystals $a = \beta = 1$. The bulk modulus anisotropies along the a- and c-axes with respect to the b-axes are denoted by A_{B_a} and A_{B_c}, respectively. A_{B_a} and A_{B_c} values equal to 1 indicate isotropy. Therefore, it shows that the directional bulk modulus of M_2LiAlH_6 (M = Na, K) compounds is isotropic. The directional bulk moduli of M_2LiAlH_6 (M = Na, K) compounds that have been calculated along various crystallographic axes are equivalent. This value is larger than the isotropic polycrystalline bulk modulus.

Three-dimensional (3D) direction dependent Young modulus, linear compressibility, bulk modulus, shear [71] modulus, and Poisson's ratio should all be spherical for a mechanically isotropic solid; however, any divergence from spherical shape implies anisotropy. For Na_2LiAlH_6 and K_2LiAlH_6, the VELAS generated 3D plots showing the direction dependence of shear modulus, bulk modulus, Young's modulus, Poisson's ratio, linear compressibility, and hardness. These are shown in Fig. 2 using GGA and Fig. 3 using LDA for Na_2LiAlH_6 and K_2LiAlH_6, respectively. Figs. 2 and 3 illustrate a minor divergence from a spherical shape in the 3D representations of Young's modulus and shear modulus, indicating a certain level of anisotropy. However, the 3D representation of bulk modulus and linear compressibility exhibits no variation from a spherical shape, indicating complete isotropy. Table 6 presents the maximum and minimum values of Young's modulus, linear compressibility, shear modulus and bulk modulus, together with their ratios of maximum to minimum. These ratios provide as valuable indicators of elastic anisotropy.

3.3. Optical properties

The response of a material to incident electromagnetic radiation is associated with its optical characteristics. The reaction to visible light is particularly significant for optoelectronic applications. The reaction to incident radiation can be entirely ascertained by several energy and frequency-dependent optical characteristics, specifically the dielectric function, refractive index, loss function, optical conductivity, reflectivity, and absorption coefficient. To investigate potential anisotropy in optical properties, we computed the optical parameters of M_2LiAlH_6 (M = Na, K) for photon energies up to 40 eV, specifically for [100] polarization orientations of the input electric field. Energy-dependent density

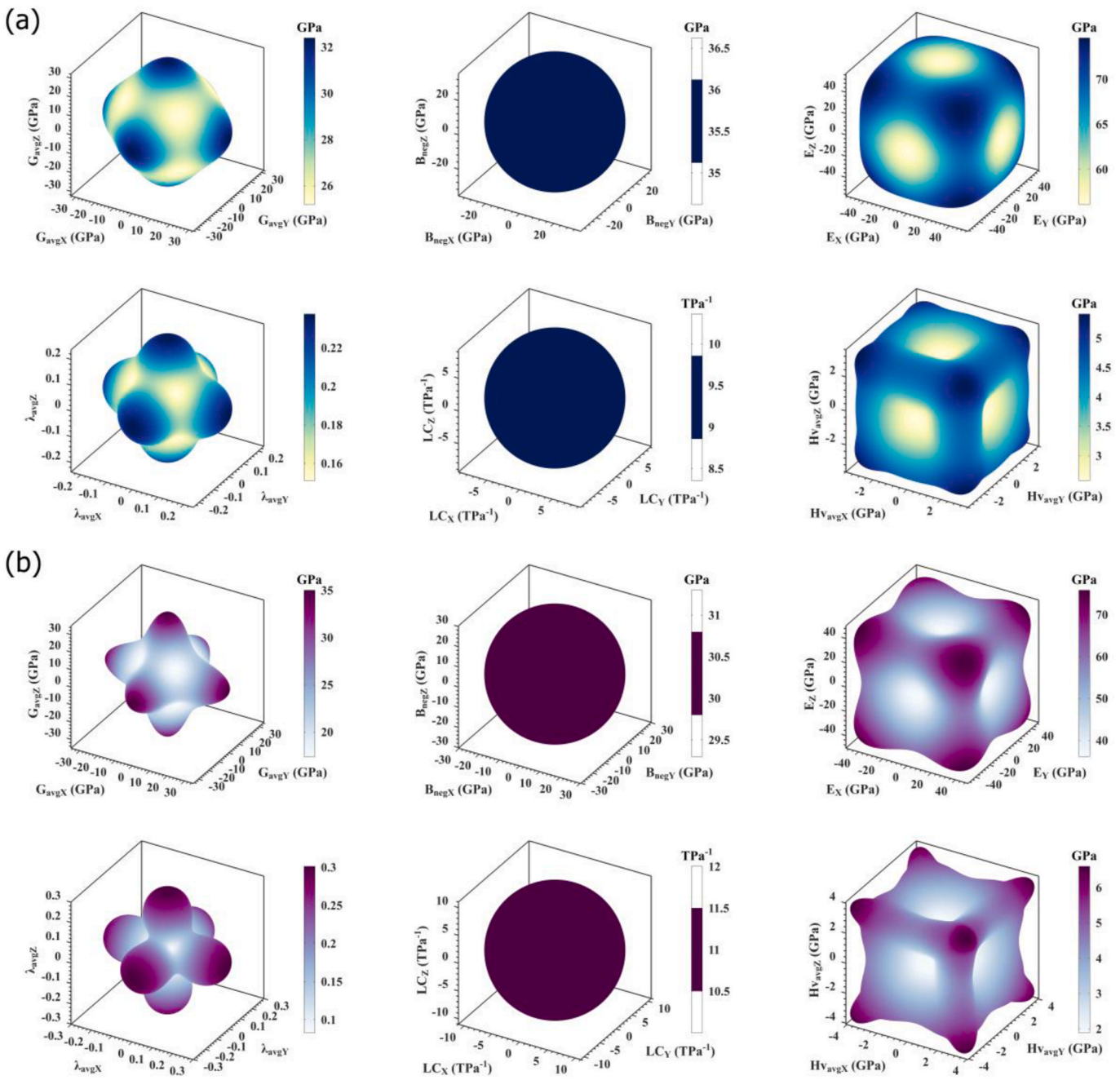

Fig. 2. Three-dimensional visualizations of the directional elastic properties of (a) **Na_2LiAlH_6,** and (b) K_2LiAlH_6 using GGA. The illustrated parameters are, respectively: shear modulus (G), bulk modulus (B), Young's modulus (E), Poisson's ratio (λ), linear compressibility (LC) and hardness (H_v).

of states characteristics and the electronic band structure linked the optical properties [72,73]. The optical properties of M_2LiAlH_6 (M = Na, K) were derived using the frequency-dependent dielectric function [74].

$$\varepsilon(\omega) = \varepsilon_1(\omega) + i\varepsilon_2(\omega) \tag{20}$$

The degree of polarization and the velocity of electromagnetic waves in the material are related to the dielectric constant's real portion. Due to frequency-dependent oscillations of the dipoles, the imaginary portion gives information about how the material absorbs energy from the entering electromagnetic field. The value of $\varepsilon(\omega)$ in the condensed matter system is influenced by both intra- and inter-band electronic transitions. Intra-band transitions are important at low energies, but the inter-band part is strongly impacted by the particular features of the electronic band structure [75]. The energy-dependent complex dielectric function $\varepsilon(\omega)$ of a material can be used to calculate its refractive index, optical reflectivity R(ω), absorption coefficient α(ω), and optical conductivity σ(ω). For the [100] polarization direction of the electric field, the determined optical characteristics of M_2LiAlH_6 (M = Na, K) for photon energies up to 40 eV are shown in Fig. 4. The ε_1 and ε_2 denote the real and imaginary parts of the dielectric function, respectively. The dielectric function characterizes a material's ability to hold an electromagnetic field and its interaction with light absorption [76,77]. The value of static dielectric function $\varepsilon_1(0)$ is 3.47, 3.82, 2.94 and 3.14 for Na_2LiAlH_6 (GGA), Na_2LiAlH_6 (LDA), K_2LiAlH_6 (GGA) and K_2LiAlH_6 (LDA) respectively. This suggests that the polarizability of Na_2LiAlH_6 is higher. The maximum values of $\varepsilon_1(\omega)$ for Na_2LiALH_6 (GGA), Na_2LiALH_6 (LDA), K_2LiALH_6 (GGA), and K_2LiALH_6 (LDA) are 8.65, 9.43, 8.79 and 7.54 at 5.5.2 eV, respectively, according to Fig. 4(a)

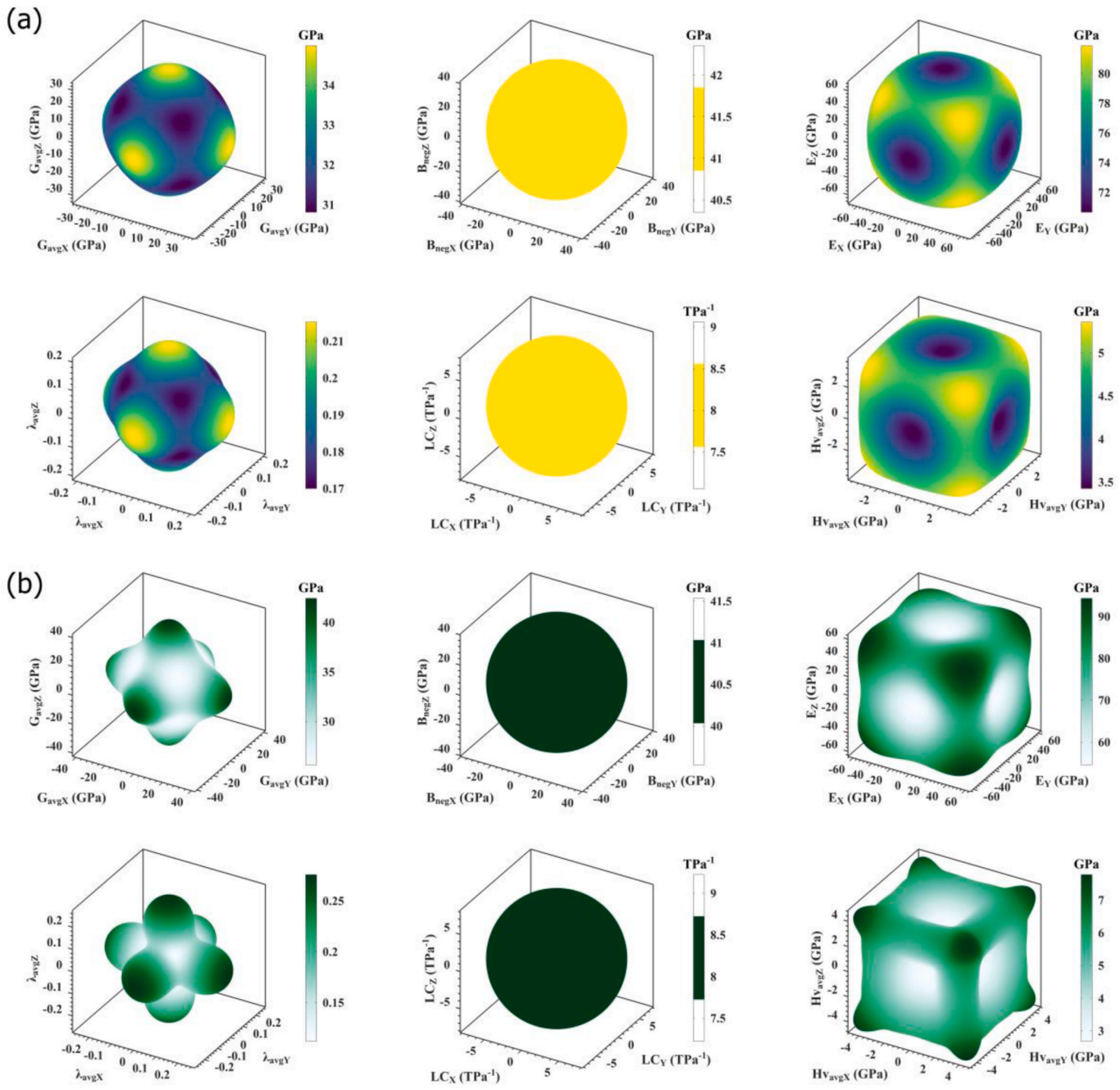

Fig. 3. Three-dimensional visualizations of the directional elastic properties of (a) Na_2LiAlH_6, and (b) K_2LiAlH_6 using LDA. The illustrated parameters are, respectively: shear modulus (G), bulk modulus (B), Young's modulus (E), Poisson's ratio (λ), linear compressibility (LC) and hardness (H_v).

Table 6
Maximum, minimum, and anisotropy values of Young's modulus (E), linear compressibility (β), shear modulus (G) and bulk modulus (B) values for **Na_2LiAlH_6,** and K_2LiAlH_6 using both GGA and LDA.

Compound	E_{max}	E_{min}	A_E	β_{max}	β_{min}	A_β	G_{max}	G_{min}	A_G	B_{max}	B_{min}	A_B
Na_2LiAlH_6 (GGA)	74.57	56.10	0.08	9.36	9.36	0.00	32.39	22.67	0.98	35.62	35.62	0.00
Na_2LiAlH_6 (LDA)	81.58	70.66	0.04	8.06	8.06	0.00	34.99	29.07	0.05	41.35	41.35	0.00
K_2LiAlH_6 (GGA)	75.82	36.14	0.21	11.00	11.00	0.00	35.01	13.89	0.26	30.30	30.30	0.00
K_2LiAlH_6 (LDA)	94.34	54.55	0.16	8.22	8.22	0.00	42.42	21.38	0.19	40.53	40.53	0.00

and (b).

The refractive index, n(ω), measures the deviation of light as it passes through a compound. It provides information on the electromagnetic wave's phase velocity and level of propagation in a medium. Fig. 4(c) indicates that the static refractive index n (0) at zero frequency is 1.86 for Na_2LiAlH_6 (GGA), 1.96 for Na_2LiAlH_6(LDA), 1.72 for K_2LiAlH_6 (GGA), and 1.78 for K_2LiAlH_6 (LDA). The refractive index, n(ω), increases in the ultraviolet region, reaching its peak values at specific

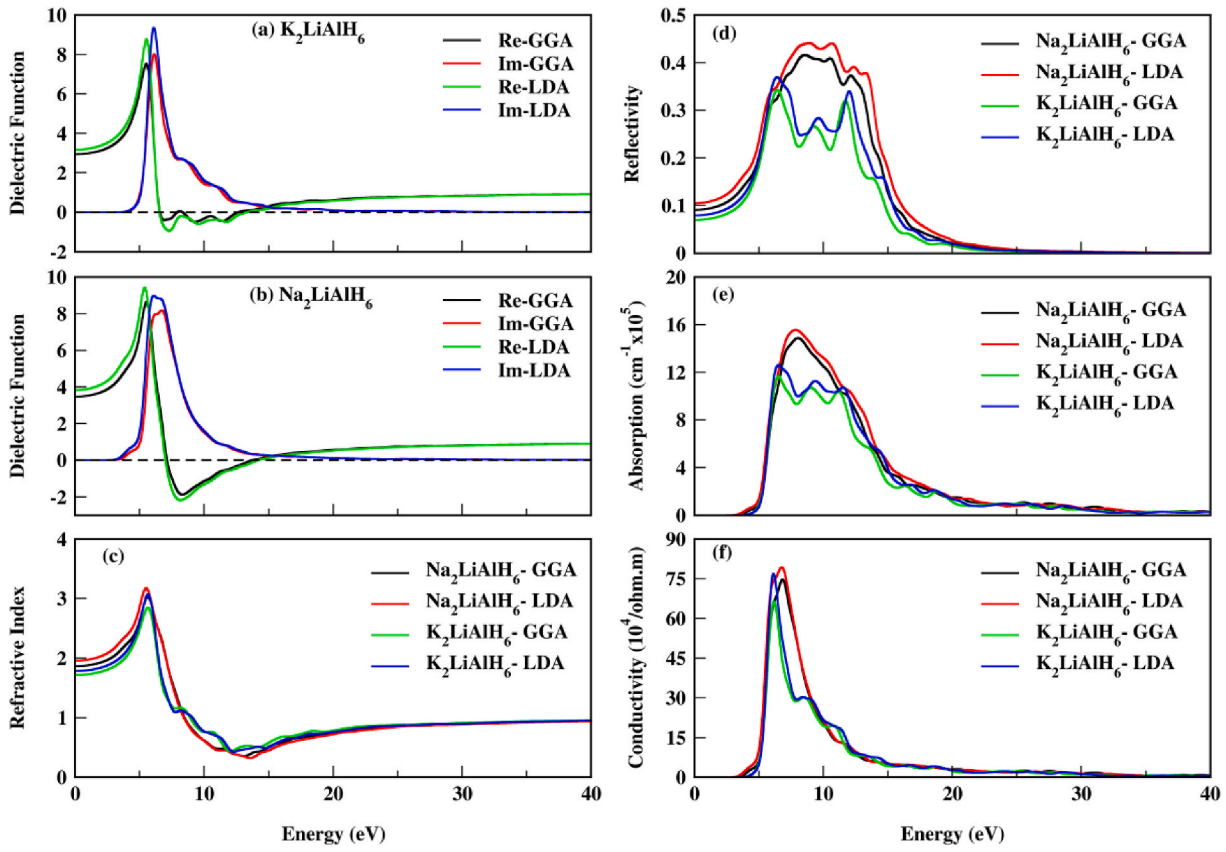

Fig. 4. Real and imaginary part of dielectric function for (a) K_2LiAlH_6, and b) Na_2LiAlH_6. (c) Refractive index, (d) Reflectivity, (e) Absorption coefficient, and (f) Conductivity as a function of energy for K_2LiAlH_6, and Na_2LiAlH_6.

energy levels for various compounds: 3.03 at 5.60 eV for Na_2LiAlH_6 (GGA), 3.18 at 5.52 eV for Na_2LiAlH_6 (LDA), 2.85 at 5.68 eV for K_2LiAlH_6 (GGA), and 3.07 at 5.68 eV for K_2LiAlH_6 (LDA). The elevated value of n(ω) for Na_2LiAlH_6 indicates a significant deceleration of light waves due to electric polarization, resulting in an augmented refractive index.

The ratio of reflected power to incident power on a material's surface is described by the reflectivity or reflection coefficient, also known as R (ω), which is a significant optical characteristic. It measures the amount of incident light that is reflected off the material's surface. By regulating the quantity of light that is reflected or transmitted through a material's surface, reflectivity can be used to improve the efficiency and performance of optical devices [78]. The static reflectance values R(0) for Na_2LiAlH_6 (GGA), Na_2LiAlH_6 (LDA), K_2LiAlH_6 (GGA), and K_2LiAlH_6 (LDA) are 9 %, 10 %, 7 %, and 8 %, respectively, as determined by Fig. 4 (d). Maximum reflectance R(ω) is measured for Na_2LiAlH_6 (GGA) at 42 % at 8.48 eV, Na_2LiAlH_6 (LDA) at 44 % at 8.96 eV, K_2LiAlH_6 (GGA) at 34 % at 6.48 eV, and Na_2LiAlH_6 (LDA) at 37 % at 6.40 eV. The compounds exhibit low reflection in the visible range and strong reflectance in the UV, according to the reflectivity values derived from Fig. 4(d).

The quantity of light absorbed by an optical system over a specific distance in a material is measured by the absorption coefficient of that substance. The amount of light that is absorbed by the material and does not pass through it is determined by the absorption coefficient. Low absorption coefficient materials are transparent to light, meaning that most incident light passes through unaltered, and are therefore thought to be poor absorbers. However, materials with high absorption coefficients can absorb a large amount of light, which lowers the amount of light that is transmitted. It is essential for figuring out a substance's optical characteristics, such as how transparent or opaque it is to various light wavelengths [79,80]. The absorption coefficient for the compounds under investigation, M_2LiAlH_6 (M = Na, K), are shown in Fig. 4 (e). The absorption coefficient reaches a maximum at 14.89×10^5 cm^{-1} at 8.08 eV for Na_2LiAlH_6 (GGA), 15.57×10^5 cm^{-1} at 7.84 eV for Na_2LiAlH_6 (LDA), 11.66×10^5 cm^{-1} at 6.48 eV for K_2LiAlH_6 (GGA), and 12.60×10^5 cm^{-1} 1 at 6.56 eV for K_2LiAlH_6 (LDA). These compounds are capable of efficiently absorbing light in the ultraviolet spectrum, as seen by the abundance of peaks in the higher photon energy range of 5–10 eV.

The ability of a substance to conduct electricity in response to electromagnetic radiation, especially in the optical frequency range, is known as optical conductivity. It measures the connection between the radiation-induced current density and the applied electric field. Optical conductivity for M_2LiAlH_6 (M = Na, K) compounds are shown in Fig. 5 (f). Maximum optical conductivities for Na_2LiAlH_6 (GGA), Na_2LiAlH_6 (LDA), K_2LiAlH_6 (GGA) and K_2LiAlH_6 (LDA) were obtained at 6.84, 6.80, 6.16 and 6.16 eV, respectively. Furthermore, the value of σ(ω) decreases with increasing photonic energy above 7 eV. Moreover, it is obvious that the optical conduction of the substances happens solely in the ultraviolet region and is not prevalent in the visible spectrum. This indicates that the compound's electrons would not be stimulated by incident photons in the visible spectrum.

3.4. *Electronic properties*

The electronic characteristics of M_2LiAlH_6 (M = Na, K) were examined by band structure and density of states (DOS) calculations, employing both GGA and LDA approximations. These features offer significant insights into the electronic and optical characteristics of the materials. In solid-state physics, electronic band structures are essential for comprehending the properties of different materials. They clarify the distribution of energy levels at symmetrical places and significantly affect a material's magnetic, electrical, and thermal properties. The predicted electronic band structure and high symmetry directions

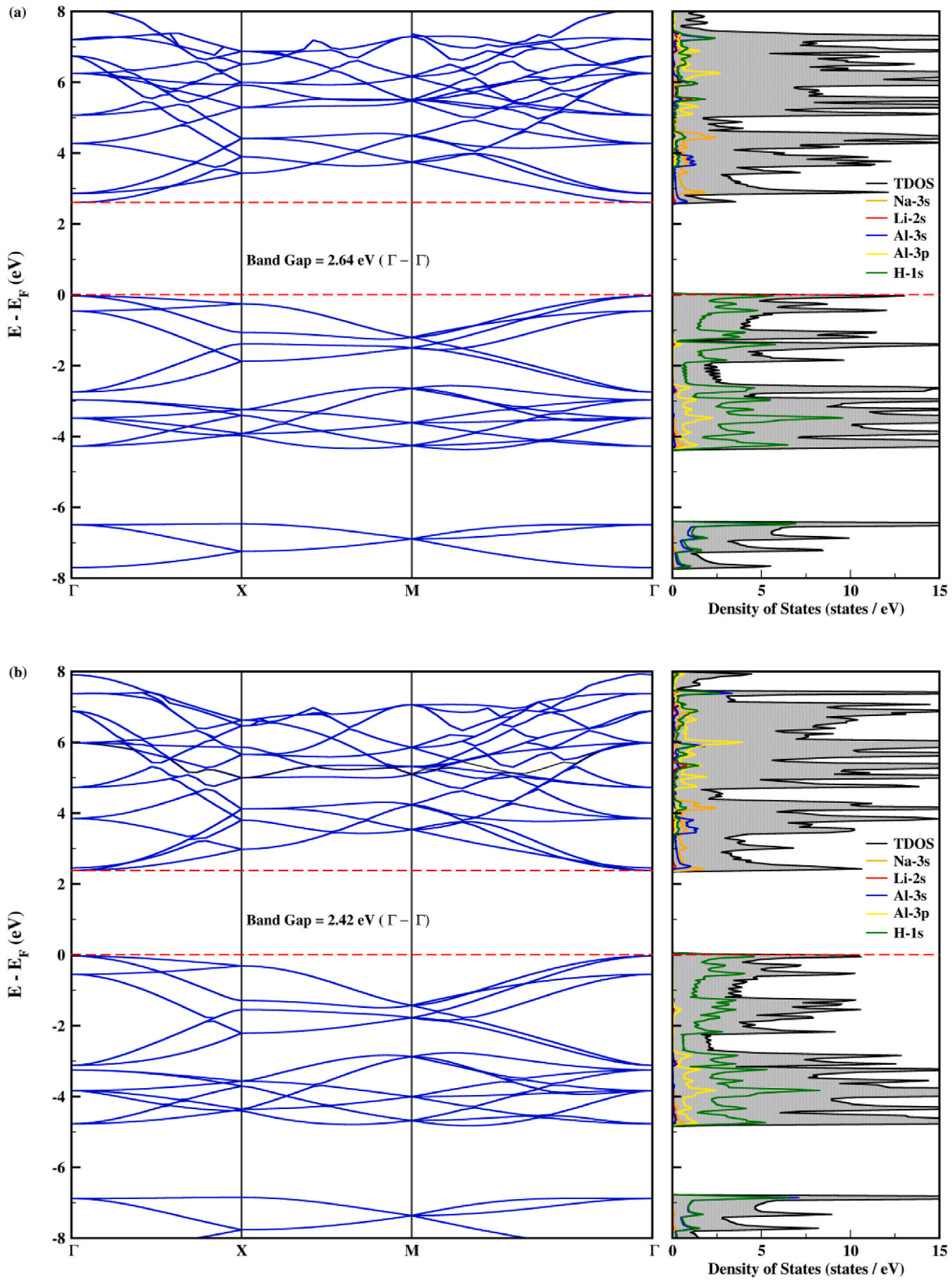

Fig. 5. The calculated energy band structures with density of states for (a) Na_2LiAlH_6 (GGA), (b) Na_2LiAlH_6 (LDA), (c) K_2LiAlH_6 (GGA), and (d) K_2LiAlH_6 (LDA).

within the first Brillouin zone at the equilibrium volume for M_2LiAlH_6 (M = Na, K) are shown in Fig. 5(a)–(d). M_2LiAlH_6 (M = Na, K) exhibits a direct band gap (Γ-Γ), with the conduction band minimum and valence band maximum both located at Γ-symmetry. The band gaps for Na_2LiAlH_6 (GGA), Na_2LiAlH_6 (LDA), K_2LiAlH_6 (GGA) and K_2LiAlH_6 (LDA) were obtained as 2.64 eV, 2.42 eV, 2.44 eV and 2.33 eV,

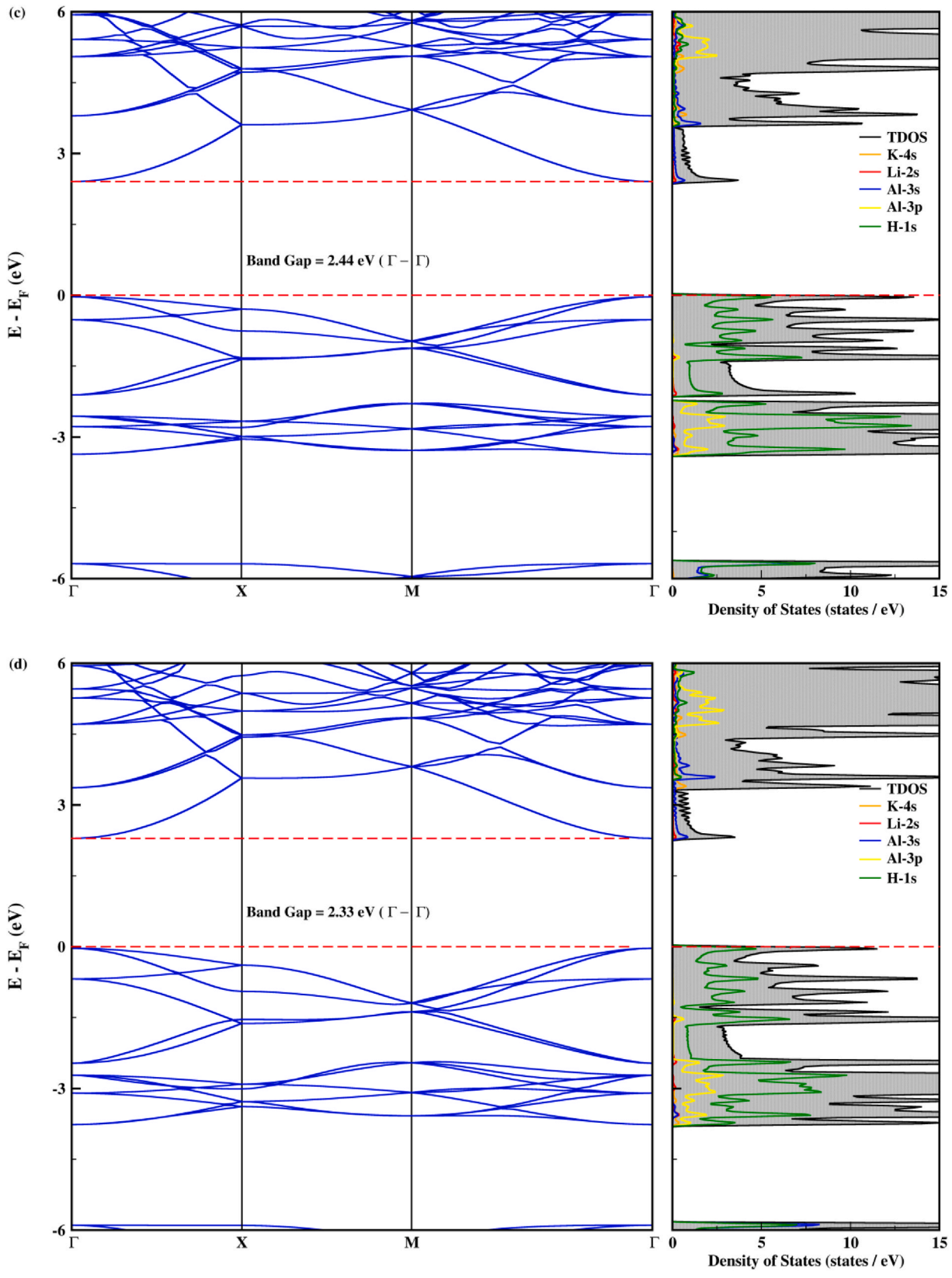

Fig. 5. (*continued*).

respectively. Furthermore, M_2LiAlH_6 (M = Na, K) compounds can be said to exhibit semiconductor properties with wide band gaps. These compounds have potential applications in energy storage devices and the semiconductor industry due to their electronic band gap. There are no experimental findings in the literature to compare the band gap results, but they are in agreement with the theoretical study of Pan et al. [36]. Consequently, our research may provide a basis for subsequent investigations into these compounds.

The total density of states (TDOS) and partial density of states (PDOS) investigations offer significant insights into the electronic structure of materials, elucidating the distribution of potential states for the system's electrons. It enables the analysis of the composition and structure of both the valence and conduction bands, elucidating the bonding qualities and features of the material. For the Na_2LiAlH_6 compound, according to both the GGA and LDA approach, it is seen in Fig. 5 (a) and (b) that the largest contributions in the conduction band in the upper part of the fermi level up to 5 eV are due to Na-3s and Al-3s, while the largest contributions in the 5 eV–8 eV range are due to Al-3p and H-1s. In the valence band in the lower region of the Fermi level, the largest contribution is observed from H-1s. For the K_2LiAlH_6 compound, according to both the GGA and LDA approach, it is seen in Fig. 5 (c) and (d) that the largest contribution in the conduction band up to 5 eV is due to Al-3s and the largest contribution in the 5 eV–6 eV range is due to Al-3p. In the valence band, the largest contribution is observed from H-1s.

3.5. Phonon dynamics

We calculated the phonon dispersion spectra of M_2LiAlH_6 (M = Na, K) compounds in the Brillouin zone along Γ-X-*M*-Γ using the GGA (PBE) and LDA (CA) approaches. We used a density functional perturbation theory-based finite displacement method (DFPT) to execute this calculation [81]. The characteristics of phonons are crucial for comprehending crystal materials. The phonon distribution spectra elucidate a material's phase transition, structural stability, and the influence of vibrations [82]. The PHONOPY software [83] was used to implement the finite displacement method that we used in our work to find phonon dispersions. Fig. 6 illustrates the computed phonon dispersion curves along high-symmetry directions within the Brillouin zone of M_2LiAlH_6 (M = Na, K) compounds. The dispersion curves presented in Fig. 6 (c) and (d) for K_2LiAlH_6 provide no indication of a negative frequency branch. This indicates that K_2LiAlH_6 crystals exhibit dynamic stability at zero pressure. However, it is seen from Fig. 6 (a) and (b) that there are

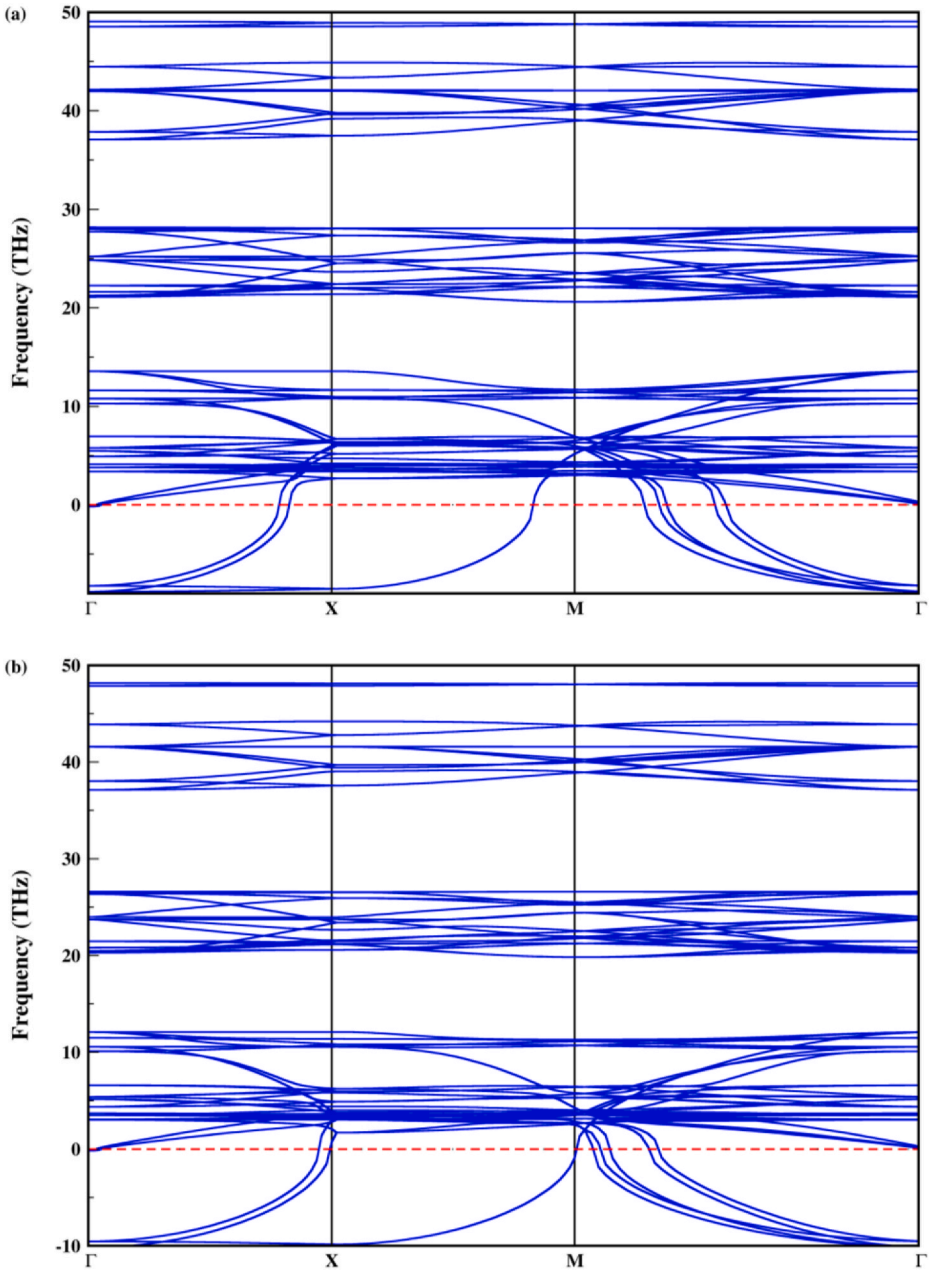

Fig. 6. The phonon dispersion curves for (a) Na_2LiAlH_6 (GGA), (b) Na_2LiAlH_6 (LDA), (c) K_2LiAlH_6 (GGA), and (d) K_2LiAlH_6 (LDA).

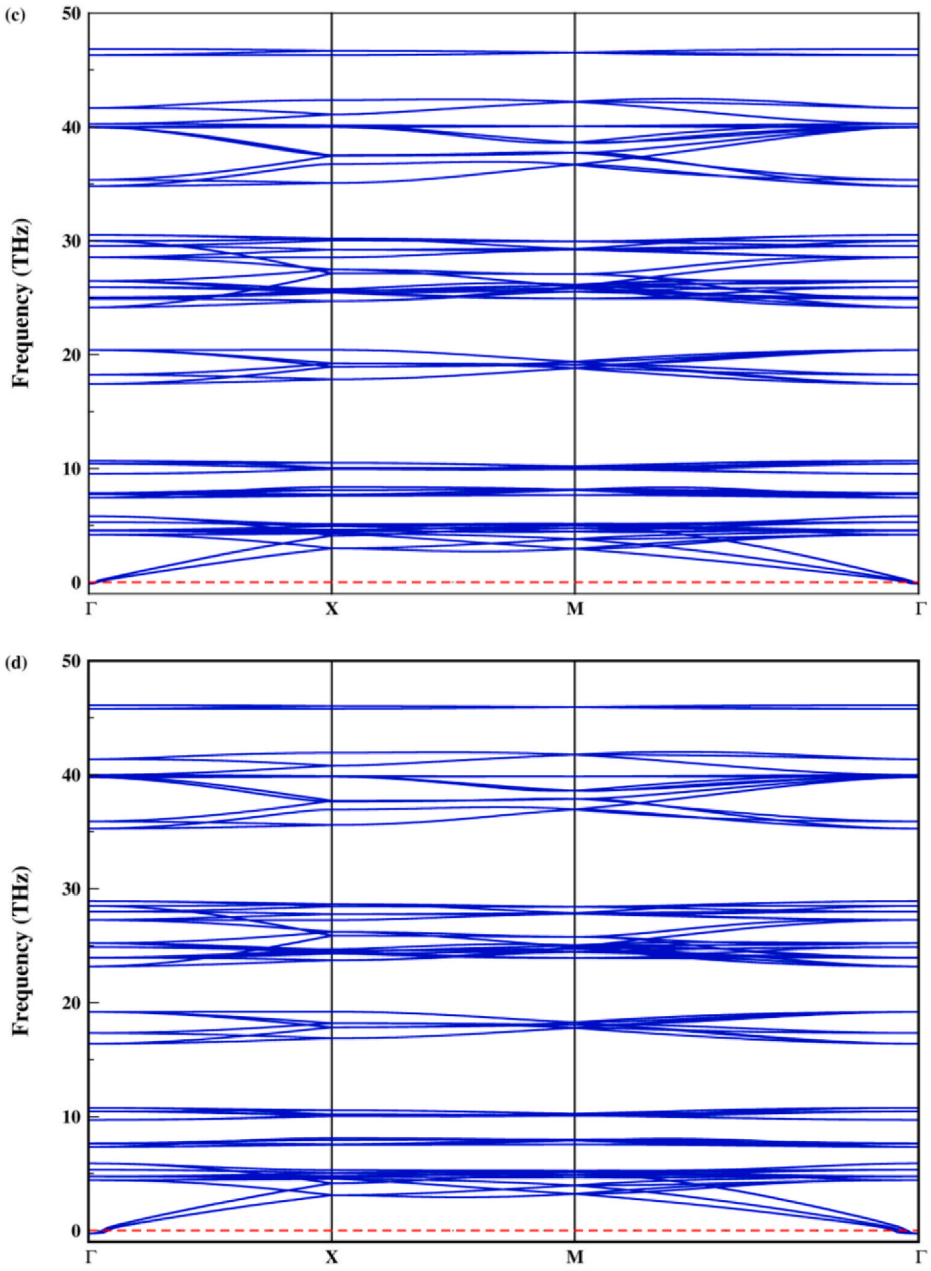

Fig. 6. (*continued*).

negative frequency branches for the Na_2LiAlH_6 compound. Therefore, Na2LiAlH6 is dynamically unstable. The result obtained for Na_2LiAlH_6 is the same as that obtained by Opalka et al. [23]. The compound K_2LiAlH_6 has 40 atoms in its unit cell. The phonon dispersion curve has a total of 120 vibrational modes, of which 3 are acoustic branches and 117 are optical branches.

3.6. Thermodynamic properties

Debye temperature (θ_D) is a crucial material characteristic that affects lattice vibration, melting temperature, thermal expansion, specific heats, and thermal conductivity. The Debye temperature is commonly used to distinguish between a solid's low and high temperature zones. The following equation is used to determine the Debye temperature [84]:

$$\theta_D = \frac{h}{k_B}\left[\left(\frac{3N}{4\pi}\right)\frac{N_A\rho}{M}\right]^{\frac{1}{3}} v_m \tag{21}$$

Here, h, k_B, N, N_A, ρ, M and v_m are Planck's constant, Boltzman's constant, number of atoms in the compound, Avagadro number, density, molar mass and average speed of sound, respectively. The moderate Debye temperature of M_2LiAlH_6 (M = Na, K) indicates that the material under study is not particularly hard and that the atomic bonding strengths are not very strong. Also, the fact that the compound Na_2LiAlH_6 has a larger Debye temperature than K_2LiAlH_6 suggests that the atomic bonds are stronger.

The following expression can be used to compute the v_m in an isotropic material given the longitudinal (v_l) and transverse (v_t) sound velocities [85]:

$$v_m = \left[\frac{1}{3}\left(\frac{2}{v_t^3} + \frac{1}{v_l^3}\right)\right]^{-\frac{1}{3}} \tag{22}$$

The values of v_l and v_t can be represented using the polycrystalline bulk modulus and shear modulus, according to the relation developed by Voigt and Reuss [86]:

$$v_l = \sqrt{\frac{3B + 4G}{3\rho}} \quad \text{and} \quad v_t = \sqrt{\frac{G}{\rho}} \tag{23}$$

v_l and v_t are associated with bulk modulus and density. Lower density and a higher bulk modulus are indicative of larger sound velocities. The sound velocities of Na_2LiAlH_6 are higher than those of K_2LiAlH_6, which is consistent with the density and bulk modulus.

The acoustic Gruneisen constant, γ_a, is a critical thermophysical parameter that estimates the anharmonic effects of a solid. It is linked to a number of significant physical processes, such as thermal expansion, thermal conductivity, acoustic wave absorption, and the temperature dependence of elastic characteristics. The degree of anharmonicity increases as the value of γ_a increases. The following equation can be used to estimate the Grüneisen parameter of M_2LiAlH_6 (M = Na, K) using acoustic velocities [87]:

$$\gamma_a = \frac{3}{2}\left(\frac{(3v_l^2 - 4v_t^2)}{v_l^2 + 2v_t^2}\right) \tag{24}$$

An important degree of anharmonicity is suggested by a high Grüneisen constant. Na_2LiAlH_6 has the highest γ_a value of 1.24, as suggested by the data in Table 7, which suggests that it has the highest degree of nonharmonicity.

The melting temperature (T_m) is a parameter of relevance that limits the temperature range within which a solid can be applied. If a solid has a high T_m, it will demonstrate a lower coefficient of thermal expansion, a higher cohesive energy, a higher bonding energy, and a stronger atomic interaction [88,89]. Using elastic constants, the melting point of a material can be ascertained using the empirical relationship below [89].

$$T_m = 354 + 1.5(2C_{11} + C_{33}) \tag{25}$$

The soft character of M_2LiAlH_6 compounds is evident in the low estimated melting temperatures. It is also observed that the melting point of the compound Na_2LiAlH_6 is higher than that of K_2LiAlH_6. Consequently, Na_2LiAlH_6 will possess a higher cohesive and bonding energy than K_2LiAlH_6.

The minimal thermal conductivity (K_{min}) is the lowest value that a compound's inherent lattice thermal conductivity approaches at high temperatures. The significance of this parameter is that it is not influenced by the presence of defects, impurities, or imperfections in the crystal. Clarke devised the equation which follows to estimate the K_{min} at high temperatures by employing the quasi-harmonic Debye model [90]:

$$K_{min} = k_B v_m \left(\frac{M}{n\rho N_A}\right)^{-\frac{2}{3}} \tag{26}$$

The compound with the highest Debye temperature demonstrates the highest melting point and the greatest hardness. This outcome is anticipated, as an elevated Debye temperature signifies a more robust interatomic connection, leading to a higher melting point and enhanced mechanical strength. The computed Debye temperatures for M_2LiAlH_6 (M = Na, K) are typically low, indicating the intrinsic softness of these material.

The thermal characteristics of M_2LiAlH_6 (M = Na, K) compounds within the temperature range of 0–2000 K are illustrated in Fig. 7. The internal energy (E) increases with temperature for all materials, as illustrated in Fig. 7(d). Conversely, the free energy (F) of M_2LiAlH_6 (M = Na, K) materials decreases monotonically with an increase in temperature, as depicted in Fig. 7(a). The reduction in F is contingent upon the entropy of the M_2LiAlH_6 (M = Na, K) materials, which escalates with rising temperature, as illustrated in Fig. 7 (b). The rise in entropy is attributable to the disorderness in compounds when temperature escalates. Fig. 7 (c) depicts the heat capacity at constant volume (C_V) of M_2LiAlH_6 (M = Na, K) materials, which helps to determine how successfully these compounds store heat. At temperatures above 750 K, the C_V becomes constant, anticipating the excitation of all phonons above this temperature and complying with the Dulong-Petit law.

3.7. Hydrogen storage properties

A primary obstacle in the adoption of hydrogen as a fuel is the lack of effective methods for storing hydrogen that provide a sufficient gravimetric storage ratio for practical efficiency. A compelling strategy for resolving this issue is the creation of materials capable of reversibly storing hydrogen at high concentrations [91,92]. Hydrogen storage techniques are categorized into three primary types: solid-state hydrogen, liquid hydrogen, and gaseous hydrogen. A diverse array of chemicals has been computed for this purpose, including bialkali alanates. The maximal hydrogen storage capacity of M_2LiAlH_6 (M = Na, K) compounds has been assessed by the examination of both gravimetric and volumetric storage capacities. The bialkali alanates Na_2LiAlH_6 and K_2LiAlH_6 have negative formation energies, as indicated in Table I, signifying that these materials are chemically more stable and potentially amenable to experimental synthesis [46,93]. Gravimetric ($C_{wt\%}$) and volumetric (C_v) storage capacities were determined to investigate the suitability of M_2LiAlH_6 (M = Na, K) compounds as candidate hydrogen storage materials. Equation (27) was used to calculate the gravimetric storage capacities of M_2LiAlH_6 (M = Na, K) compounds [94].

$$C_{wt\%} = \left(\frac{\left(\frac{H}{M}\right)M_H}{M_{Host} + \left(\frac{H}{M}\right)M_H} x\,100\right)\% \tag{27}$$

In Equation (27), H/M represents the hydrogen to metal ratio, M_H represents hydrogen's molecular weight, and M_{Host} represents the molecular weight of the host material. The $C_{wt\%}$ and C_v values for M_2LiAlH_6 (M = Na, K) compounds are presented in Table 8. The reported gravimetric storage capacities of Na_2LiAlH_6 and K_2LiAlH_6 materials are 3.42 % and 2.50 %, respectively. Furthermore, we have established the C_v values for the molecules Na_2LiAlH_6 and K_2LiAlH_6 as 100.63 and 83.10 gH_2l^{-1}, respectively. As a result, the Na_2LiAlH_6 compound has a higher storage capacity than the K_2LiAlH_6 compound. The US Department of Energy's objective for 2025 is a gravimetric storage capacity of 5.5 % and a volumetric storage capacity of 40 gH_2l^{-1}. The volumetric storage capacity of Na_2LiAlH_6 and K_2LiAlH_6 compounds surpasses the US Department of Energy's target of 40 gH_2l^{-1} for practical applications.

The desorption temperature (T_{des}) is a critical parameter for

Table 7
Calculated mass density (ρ in g cm^{-3}), transverse, longitudinal, and sound velocities (v_t, v_l, and v_m in m s^{-1}, respectively), melting temperature (T_m in K), Debye temperature (θ_D in K), minimum thermal conductivity (K_{min} in Wm^{-1} K^{-1}), and Grüneisen constant (γ_a) of for **Na_2LiAlH_6,** and K_2LiAlH_6 using both GGA and LDA.

Compound	ρ	v_t	v_l	v_m	T_m	θ_D	K_{min}	γ_a
Na_2LiAlH_6 (GGA)	1.44	4412.51	7117.86	4865.09	650.30	674.52	1.46	1.24
Na_2LiAlH_6 (LDA)	1.56	4566.70	7372.21	5035.50	714.56	716.39	1.59	1.24
K_2LiAlH_6 (GGA)	1.64	3842.11	6179.87	4234.88	573.67	550.83	1.12	1.23
K_2LiAlH_6 (LDA)	1.80	4226.39	6803.41	4658.84	664.70	625.92	1.31	1.23

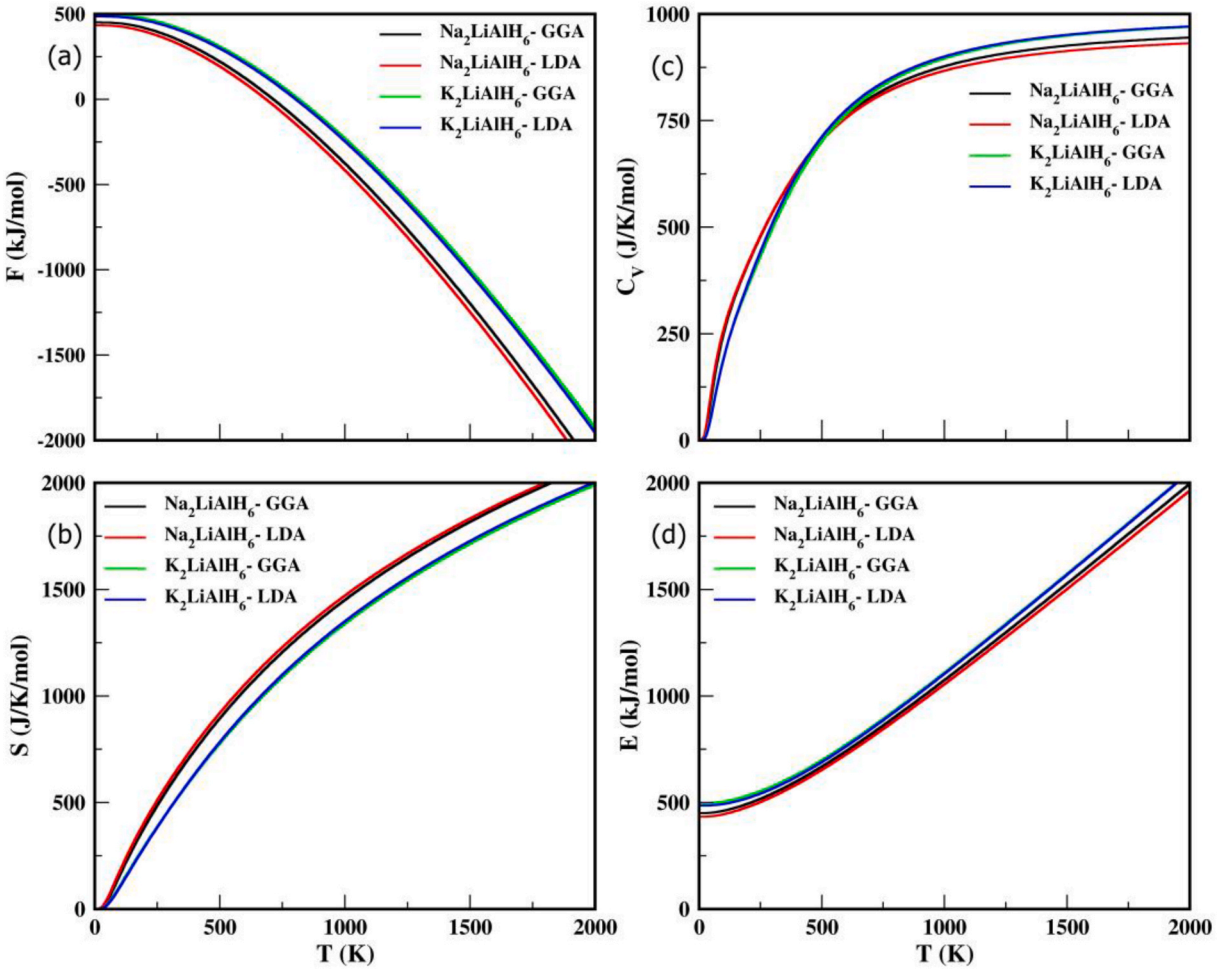

Fig. 7. Calculated (a) free energy (F), (b) entropy (S), (c) heat capacity (C_v), and (d) energy (E) as a function of temperature of K_2LiAlH_6, and Na_2LiAlH_6.

Table 8
Calculated desorption temperature [T_{des} (K)], gravimetric [$C_{wt\%}$] and volumetric [C_v (gH_2l^{-1})] storage capacities for **Na_2LiAlH_6,** and K_2LiAlH_6.

Compound	T_{des}	$C_{wt\%}$	C_v
Na_2LiAlH_6	256.88	3.42	100.63
K_2LiAlH_6	281.46	2.50	83.10

hydrogen storage applications. T_{des} can be determined using the subsequent equation [95].

$$T_{des} = \frac{\Delta S}{\Delta H} \tag{28}$$

The generation of hydrogen gas (H_2) is the primary component influencing the alteration in entropy during the decomposition process. The prevailing view among scientific professionals and published literature is that the change in entropy (ΔS) for H_2 is around −130.7 J/mol·K at conventional temperature and pressure situations [96]. ΔH represents the enthalpy of formation energy derived from Equation (1). The desorption temperature values for Na_2LiAlH_6, and K_2LiAlH_6 are 256.88K and 281.46K, respectively. The desorption temperature values obtained fall within the designated range of T_{des} (233–333 K) established by the United States Department of Energy for the year 2025 [97,98].

4. Conclusion

In this study, the structural, mechanical, electronic, phonon, optical, thermodynamic, and hydrogen storage properties of M_2LiAlH_6 (M = Na, K) compounds were systematically investigated using first-principles DFT methods. Both compounds crystallize in a cubic structure and are thermodynamically stable, with negative formation enthalpies (Na_2LiAlH_6: 0.348 eV/atom; K_2LiAlH_6: 0.381 eV/atom). Elastic constants confirmed mechanical stability, though negative Cauchy pressures and Pugh's ratios below 1.75 indicate brittleness. Na_2LiAlH_6 exhibits higher hardness and stiffness than K_2LiAlH_6.

Electronic band structure analysis revealed direct bandgaps at the Γ-point (2.64 eV for Na_2LiAlH_6 and 2.44 eV for K_2LiAlH_6), confirming their semiconducting nature. Phonon calculations indicated that only K_2LiAlH_6 is dynamically stable, as Na_2LiAlH_6 displayed imaginary frequencies. Optical analyses showed strong UV activity, with peak reflectivity values of 42 % (Na_2LiAlH_6) and 34 % (K_2LiAlH_6), alongside high absorption coefficients in the UV region.

Thermal analyses revealed higher Debye temperature and melting point for Na_2LiAlH_6, implying stronger atomic bonding. Importantly, hydrogen storage evaluations showed that Na_2LiAlH_6 meets the DOE 2025 volumetric target with 100.63 gH_2/L and a gravimetric capacity of 3.42 wt%, outperforming K_2LiAlH_6.

CRediT authorship contribution statement

Çağatay Yamçıçır: Writing – original draft, Methodology, Investigation. **Cihan Kürkçü:** Writing – original draft, Supervision, Methodology, Investigation.

Declaration of competing interest

The authors declare that they have no known competing financial interests or personal relationships that could have appeared to influence the work reported in this paper.

Acknowledgment

This study was supported by the Kırşehir Ahi Evran University under Scientific Research Project No: TBY.A1.24.001.

References

[1] Wei TY, Lim KL, Tseng YS, Chan SLI. A review on the characterization of hydrogen in hydrogen storage materials. Renew Sustain Energy Rev 2017;79:1122–33. https://doi.org/10.1016/j.rser.2017.05.132.
[2] Züttel A. Materials for hydrogen storage. Mater Today 2003;6:24–33. https://doi.org/10.1016/S1369-7021(03)00922-2.
[3] Niaz S, Manzoor T, Pandith AH. Hydrogen storage: materials, methods and perspectives. Renew Sustain Energy Rev 2015;50:457–69. https://doi.org/10.1016/j.rser.2015.05.011.
[4] Yamçıçır Ç, Kürkçü C. Ab initio study of the structural, mechanical, optoelectronic and thermo-physical properties of XGaH5 (X=Ba, Ca, and Mg) compounds for hydrogen storage applications. Int J Hydrog Energy 2024;81:391–404. https://doi.org/10.1016/j.ijhydene.2024.07.276.
[5] Yamçıçır Ç, Kürkçü C. Investigation of structural, electronic, elastic, vibrational, thermodynamic, and optical properties of Mg2NiH4 and Mg2RuH4 compounds used in hydrogen storage. J Energy Storage 2024;84:110883. https://doi.org/10.1016/j.est.2024.110883.
[6] Brinks H, Hauback B, Jensen C, Zidan R. Synthesis and crystal structure of Na2LiAlD6. J Alloys Compd 2005;392:27–30.
[7] Formation Reactions and the Thermodynamics and Kinetics of Dehydrogenation Reaction of Mixed Alanate Na2LiAlH6 | J Phys Chem C 113(18):7978–7984. https://pubs.acs.org/doi/abs/10.1021/jp9011697.
[8] Graetz J, Lee Y, Reilly JJ, Park S, Vogt T. Structures and thermodynamics of the mixed alkali alanates. Phys Rev B 2005;71:184115. https://doi.org/10.1103/PhysRevB.71.184115.
[9] Wang K, Zhang X, Wang F. First-principles investigations on the elastic properties, thermodynamic properties, electronic structures and anisotropy sound velocity of AlTi3N, AlTi2N, AlTi4N3 and Al2Ti3N2 ternary nitrides. Chem Phys Lett 2025;865:141930. https://doi.org/10.1016/j.cplett.2025.141930.
[10] Wang K, Zhang X, Wang F. Impact of TM elements (TM=Cr, Mn, Ti, Sc) doped on the electronic and mechanical properties of ZrAlNi intermetallics. Phys Lett A 2025;533:130215. https://doi.org/10.1016/j.physleta.2024.130215.
[11] Tian M, Zhang X, Wang F. Structural, mechanical, electronic and thermodynamic properties of YBC, YB2C, YB2C2, Y2B3C2 intermetallics. Mater Today Commun 2024;39:108696. https://doi.org/10.1016/j.mtcomm.2024.108696.
[12] Ali NA, Ismail M. Modification of NaAlH4 properties using catalysts for solid-state hydrogen storage: a review. Int J Hydrog Energy 2021;46:766–82. https://doi.org/10.1016/j.ijhydene.2020.10.011.
[13] Sazelee NA, Ismail M. Recent advances in catalyst-enhanced LiAlH4 for solid-state hydrogen storage: a review. Int J Hydrog Energy 2021;46:9123–41. https://doi.org/10.1016/j.ijhydene.2020.12.208.
[14] Häussermann U, Blomqvist H, Noréus D. Bonding and stability of the hydrogen storage material Mg2NiH4. Inorg Chem 2002;41:368492. https://pubs.acs.org/doi/abs/10.1021/ic0201046.
[15] Ordejón P, Artacho E, Soler JM. Self-consistent order-N density-functional calculations for very large systems. Phys Rev B 1996;53:R10441–4. https://doi.org/10.1103/PhysRevB.53.R10441.
[16] Perdew JP, Burke K, Ernzerhof M, Perdew Burke, Reply Ernzerhof. Phys Rev Lett 1998;80:891. https://doi.org/10.1103/PhysRevLett.80.891. 891.
[17] Ceperley DM, Alder BJ. Ground state of the electron gas by a stochastic method. Phys Rev Lett 1980;45:566–9. https://doi.org/10.1103/PhysRevLett.45.566.
[18] Negele JW. Structure of finite nuclei in the local-density approximation. Phys Rev C 1970;1:1260–321. https://doi.org/10.1103/PhysRevC.1.1260.
[19] Troullier N, Martins JL. Efficient pseudopotentials for plane-wave calculations. Phys Rev B 1991;43:1993–2006. https://doi.org/10.1103/PhysRevB.43.1993.
[20] Monkhorst HJ, Pack JD. Special points for Brillouin-zone integrations. Phys Rev B 1976;13:5188–92. https://doi.org/10.1103/PhysRevB.13.5188.
[21] Momma K, Izumi F. VESTA: a three-dimensional visualization system for electronic and structural analysis. J Appl Crystallogr 2008;41:653–8. https://doi.org/10.1107/S0021889808012016.
[22] Mouhat F, Coudert F-X. Necessary and sufficient elastic stability conditions in various crystal systems. Phys Rev B 2014;90:224104. https://doi.org/10.1103/PhysRevB.90.224104.
[23] Opalka SM, Løvvik OM, Brinks HW, Saxe PW, Hauback BC. Integrated Experimental–Theoretical investigation of the Na–Li–Al–H system. Inorg Chem 2007;46:1401–9. https://doi.org/10.1021/ic062032e.
[24] Fossdal A, Brinks HW, Fonneløp JE, Hauback BC. Pressure–composition isotherms and thermodynamic properties of TiF3-enhanced Na2LiAlH6. J Alloys Compd 2005;397:135–9. https://doi.org/10.1016/j.jallcom.2005.01.012.
[25] Graetz J, Lee Y, Reilly JJ, Park S, Vogt T. Structures and thermodynamics of the mixed alkali alanates. Phys Rev B 2005;71:184115. https://doi.org/10.1103/PhysRevB.71.184115.
[26] Orimo S, Nakamori Y, Eliseo JR, Züttel A, Jensen CM. Complex hydrides for hydrogen storage. Chem Rev 2007;107:4111–32.
[27] Al S, Yamçıçır Ç. Computational exploration of hexahydride materials (K2SiH6 and Rb2SiH6); structural, mechanical, thermodynamic, optic, electronic and dynamic properties. J Energy Storage 2024;91:112033. https://doi.org/10.1016/j.est.2024.112033.
[28] Surucu G, Candan A, Gencer A, Isik M. First-principle investigation for the hydrogen storage properties of NaXH3 (X= Mn, Fe, Co) perovskite type hydrides. Int J Hydrog Energy 2019;44:30218–25. https://doi.org/10.1016/j.ijhydene.2019.09.201.
[29] Qi WH. Size, shape and structure dependent cohesive energy and phase stability of metallic nanocrystals. Solid State Commun 2006;137:536–9. https://doi.org/10.1016/j.ssc.2006.01.018.
[30] Dahbi S, Tahiri N, El Bounagui O, Ez-Zahraouy H. Importance of spin-orbit coupling on photovoltaic properties of Pb-free vacancy ordered double perovskites halides X_2TeY_6 (X = Cs , Rb , and Y = I , Br , Cl): first-principles calculations. Int J Energy Res 2022;46:8433–42. https://doi.org/10.1002/er.7631.
[31] Mouhat F, Coudert F-X. Necessary and sufficient elastic stability conditions in various crystal systems. Phys Rev B 2014;90:224104.
[32] Yamçıçır Ç. Exploring the structural, elastic, phonon, optoelectronics, and thermoelectric properties of tetragonal complex metal hydride X2MgH4 (X=K, Rb, and Cs) compounds for hydrogen storage applications. Int J Hydrog Energy 2023;48:39930–43. https://doi.org/10.1016/j.ijhydene.2023.09.177.
[33] Naher MI, Afzal MA, Naqib SH. A comprehensive DFT based insights into the physical properties of tetragonal superconducting Mo5PB2. Results Phys 2021;28:104612.
[34] Barua S, Rahman Rano B, Syed IM, Naqib SH. An ab initio approach to understand the structural, thermophysical, electronic, and optical properties of binary silicide SrSi2: a double Weyl semimetal. Results Phys 2022;42:105973. https://doi.org/10.1016/j.rinp.2022.105973.
[35] Kleinman L. Deformation potentials in silicon. I. Uniaxial strain. Phys Rev 1962;128:2614.
[36] Pan R-K, Yao J-G, Ji R-L, Liu W-W, Yin D-F. First principles study on elastic and electronic properties of bialkali alanates M2M′AlH6. Int J Hydrog Energy 2018;43:3862–70. https://doi.org/10.1016/j.ijhydene.2018.01.006.
[37] Ahmed R, Mahamudujjaman M, Afzal MA, Islam MS, Islam R, Naqib S. DFT based comparative analysis of the physical properties of some binary transition metal carbides XC (X= Nb. Ta, Ti). J Mater Res Technol 2023;24:4808–32.
[38] Das K, Ali M, Hossain M, Naqib S, Islam A, Uddin M. Dynamical stability, vibrational, and optical properties of anti-perovskite A3BX (Ti3TlN, Ni3SnN, and Co3AlC) phases: a first principles study. AIP Adv 2020;10.
[39] Pettifor DG. Theoretical predictions of structure and related properties of intermetallics. Mater Sci Technol 1992;8:345–9.
[40] Ravindran P, Fast L, Korzhavyi PA, Johansson B, Wills J, Eriksson O. Density functional theory for calculation of elastic properties of orthorhombic crystals: application to TiSi 2. J Appl Phys 1998;84:4891–904.
[41] Voigt W. Lehrbuch der kristallphysik (mit ausschluss der kristalloptik). Leipzig; Berlin: Ann Arbor Mich BG Teubner JW Edw; 1946.
[42] Reuss A. ZAMM-journal of applied mathematics and mechanics. Z Angew Math Mech 1929;9:49.
[43] Hill R. First-principles elastic constants for the hcp transition metals Fe, Co, and Re at high pressure. Proc Phys Soc 1952;65:350.
[44] Al S, Yamçıçır Ç. Computational exploration of hexahydride materials (K2SiH6 and Rb2SiH6); structural, mechanical, thermodynamic, optic, electronic and dynamic properties. J Energy Storage 2024;91:112033. https://doi.org/10.1016/j.est.2024.112033.
[45] Arikan N, Al S, Iyigör A. Mechanical, electronic, thermodynamic and vibrational properties of X2MgAl (X = Sc, Ti and Y) from first principles calculations. J Mol Model 2022;28:366. https://doi.org/10.1007/s00894-022-05358-7.
[46] Al S, Cavdar N, Arikan N. Computational evaluation of comprehensive properties of MgX3H8 (X = Sc, Ti and Zr) as effective solid state hydrogen storage materials. J Energy Storage 2024;80:110402. https://doi.org/10.1016/j.est.2023.110402.
[47] Kurkcu C, Al S, Yamcicier C. Investigation of mechanical properties of KCaH3 and KSrH3 orthorhombic perovskite hydrides under high pressure for hydrogen storage applications. Eur Phys J B 2022;95:180. https://doi.org/10.1140/epjb/s10051-022-00446-2.
[48] Naher MI, Naqib SH. Structural, elastic, electronic, bonding, and optical properties of topological CaSn3 semimetal. J Alloys Compd 2020;829:154509.
[49] Yamçiçier Ç, Kürkçü C, Merdan Z. A study of structural, electronic, elastic, phonon properties, and transition mechanism of wurtzite CdTe under high pressure. Solid State Sci 2020;105:106209.
[50] Greaves GN, Greer AL, Lakes RS, Rouxel T. Poisson's ratio and modern materials. Nat Mater 2011;10:823–37.
[51] Haines J, Leger J, Bocquillon G. Synthesis and design of superhard materials. Annu Rev Mater Res 2001;31:1–23.
[52] Barua P, Hossain M, Ali M, Uddin M, Naqib S, Islam A. Effects of transition metals on physical properties of M2BC (M= V, Nb, Mo and Ta): a DFT calculation. J Alloys Compd 2019;770:523–34.
[53] Fu H, Li D, Peng F, Gao T, Cheng X. Ab initio calculations of elastic constants and thermodynamic properties of NiAl under high pressures. Comput Mater Sci 2008;44:774–8.
[54] Sun Z, Music D, Ahuja R, Schneider JM. Theoretical investigation of the bonding and elastic properties of nanolayered ternary nitrides. Phys Rev B 2005;71:193402.

[55] Vitos L, Korzhavyi PA, Johansson B. Stainless steel optimization from quantum mechanical calculations. Nat Mater 2003;2:25–8.
[56] Lincoln RC, Koliwad KM, Ghate PB. Morse-potential evaluation of second-and third-order elastic constants of some cubic metals. Phys Rev 1967;157:463.
[57] Jhi S-H, Ihm J, Louie SG, Cohen ML. Electronic mechanism of hardness enhancement in transition-metal carbonitrides. Nature 1999;399:132–4.
[58] Najrin F, Sarker MA, Neher B, Bhuiyan MMR. A comparative study of structural, elastic, electronic, thermophysical, and optical properties of cubic binary lave-phase intermetallic compounds of HfX2 (X= cr, mo, and W): an ab initio insight. Results Mater 2024;23:100610.
[59] Miao N, Sa B, Zhou J, Sun Z. Theoretical investigation on the transition-metal borides with Ta3B4-type structure: a class of hard and refractory materials. Comput Mater Sci 2011;50:1559–66. https://doi.org/10.1016/j.commatsci.2010.12.015.
[60] Chen X-Q, Niu H, Li D, Li Y. Modeling hardness of polycrystalline materials and bulk metallic glasses. Intermetallics 2011;19:1275–81. https://doi.org/10.1016/j.intermet.2011.03.026.
[61] Tian Y, Xu B, Zhao Z. Microscopic theory of hardness and design of novel superhard crystals. Int J Refract Met Hard Mater 2012;33:93–106. https://doi.org/10.1016/j.ijrmhm.2012.02.021.
[62] Teter DM. Computational alchemy: the search for new superhard materials. MRS Bull 1998;23:22–7. https://doi.org/10.1557/S0883769400031420.
[63] Mazhnik E, Oganov AR. A model of hardness and fracture toughness of solids. J Appl Phys 2019;126:125109. https://doi.org/10.1063/1.5113622.
[64] Gao X, Jiang Y, Zhou R, Feng J. Stability and elastic properties of Y–C binary compounds investigated by first principles calculations. J Alloys Compd 2014;587:819–26.
[65] Hill R. The elastic behaviour of a crystalline aggregate. Proc Phys Soc Sect A 1952;65:349. https://doi.org/10.1088/0370-1298/65/5/307.
[66] Kube CM. Elastic anisotropy of crystals. AIP Adv 2016;6:095209.
[67] Kube CM, De Jong M. Elastic constants of polycrystals with generally anisotropic crystals. J Appl Phys 2016;120:165105.
[68] Arsigny V, Fillard P, Pennec X, Ayache N. Fast and simple calculus on tensors in the log-euclidean framework. In: Duncan JS, Gerig G, editors. Med. Image comput. Comput.-Assist. Interv. – miccai 2005. Berlin, Heidelberg: Springer; 2005. p. 115–22. https://doi.org/10.1007/11566465_15.
[69] Ranganathan SI, Ostoja-Starzewski M. Universal elastic anisotropy index. Phys Rev Lett 2008;101:055504.
[70] Chung DH, Buessem WR. The elastic anisotropy of crystals. J Appl Phys 1967;38:2010–2.
[71] Ran Z, Zou C, Wei Z, Wang H. VELAS: an open-source toolbox for visualization and analysis of elastic anisotropy. Comput Phys Commun 2023;283:108540. https://doi.org/10.1016/j.cpc.2022.108540.
[72] Murtaza G, Sajid A, Rizwan M, Takagiwa Y, Khachai H, Jibran M, et al. First principles study of Mg2X (X=Si, Ge, Sn, Pb): elastic, optoelectronic and thermoelectric properties. Mater Sci Semicond Process 2015;40:429–35. https://doi.org/10.1016/j.mssp.2015.06.075.
[73] Murtaza G, Gupta SK, Seddik T, Khenata R, Alahmed ZA, Ahmed R, et al. Structural, electronic, optical and thermodynamic properties of cubic REGa3 (RE=Sc or Lu) compounds: ab initio study. J Alloys Compd 2014;597:36–44. https://doi.org/10.1016/j.jallcom.2014.01.203.
[74] Kim TJ, Byun JS, Barange N, Park HG, Kang YR, Park JC, et al. Parametrization of the optical constants of $AlAs_xSb_{1-x}$ alloys in the range 0.74-6.0 eV. J Opt Soc Korea 2014;18:359–64.
[75] Wang H, Chen Y, Kaneta Y, Iwata S. First-principles study on effective doping to improve the optical properties in spinel nitrides. J Alloys Compd 2010;491:550–9.
[76] Belhadj H, Ameri M, Abbar B, Moulay N, Bouyakoub AZ, Arbouche O, et al. Optical properties of (Pb1-xMnxS)1-yFey materials from first-principles calculations. Chin J Phys 2017;55:1032–43. https://doi.org/10.1016/j.cjph.2016.11.015.
[77] Tang T-Y, Tang Y-L. Physical and optoelectronic properties of double halide perovskites A2CuSbX6 (A = Cs, Rb, K; X = Cl, Br, I) based on first principles calculations. Chem Phys 2023;570:111897. https://doi.org/10.1016/j.chemphys.2023.111897.
[78] Jehan A, Husain M, Bibi S, Rahman N, Tirth V, Azzouz-Rached A, et al. Insight into the structural, optoelectronic, and elastic properties of AuXF3 (X= Ca, Sr) fluoroperovskites: DFT study. Opt Quantum Electron 2023;55:1242.
[79] Rahman N, Husain M, Yang J, Sajjad M, Murtaza G, Ul Haq M, et al. First principle study of structural, electronic, optical and mechanical properties of cubic fluoro-perovskites:(CdXF3, X= Y, Bi). Eur Phys J Plus 2021;136:1–11.
[80] Rahman N, Husain M, Tirth V, Algahtani A, Alqahtani H, Al-Mughanam T, et al. Appealing perspectives of the structural, electronic, elastic and optical properties of LiRCl 3 (R= Be and Mg) halide perovskites: a DFT study. RSC Adv 2023;13:18934–45.
[81] Kresse G, Furthmüller J, Hafner J. Ab initio force constant approach to phonon dispersion relations of diamond and graphite. EPL Europhys Lett 1995;32:729.
[82] Yun Y, Legut D, Oppeneer PM. Phonon spectrum, thermal expansion and heat capacity of UO2 from first-principles. J Nucl Mater 2012;426:109–14.
[83] Togo A, Chaput L, Tadano T, Tanaka I. Implementation strategies in phonopy and phono3py. J Phys Condens Matter 2023;35:353001. https://doi.org/10.1088/1361-648X/acd831.
[84] Anderson OL. A simplified method for calculating the Debye temperature from elastic constants. J Phys Chem Solids 1963;24:909–17.
[85] Anderson OL. A simplified method for calculating the debye temperature from elastic constants. J Phys Chem Solids 1963;24:909–17. https://doi.org/10.1016/0022-3697(63)90067-2.
[86] Schreiber E, Anderson OL, Soga N, Bell JF. Elastic constants and their measurement. J Appl Mech 1975;42:747–8. https://doi.org/10.1115/1.3423687.
[87] Arab F, Sahraoui FA, Haddadi K, Bouhemadou A, Louail L. Phase stability, mechanical and thermodynamic properties of orthorhombic and trigonal MgSiN2: an ab initio study. Phase Transit 2016;89:480–513. https://doi.org/10.1080/01411594.2015.1089574.
[88] Fine ME, Brown LD, Marcus HL. Elastic constants versus melting temperature in metals. Scr Metall 1984;18:951–6.
[89] Clarke DS. Communicative intent and conventionality. Sign levels. Springer; 2003. p. 67–93.
[90] Clarke DR. Materials selection guidelines for low thermal conductivity thermal barrier coatings. Surf Coat Technol 2003;163:67–74.
[91] Garberoglio G, Skoulidas AI, Johnson JK. Adsorption of gases in metal organic materials: comparison of simulations and experiments. J Phys Chem B 2005;109:13094–103.
[92] Khalil R, Hayat S, Hussain MI, Rana AM, Hussain F. DFT based first principles study of novel combinations of perovskite-type hydrides XGaH3 (X= Rb, Cs, Fr) for hydrogen storage applications. AIP Adv 2021;11.
[93] Ali M, Bibi Z, Mubashir M, Younis MW, Afzal U, El-marghany A. A computational investigation of lithium-based metal hydrides for advanced solid-state hydrogen storage. ChemistrySelect 2024;9:e202304582. https://doi.org/10.1002/slct.202304582.
[94] Pluengphon P, Tsuppayakorn-aek P, Sukmas W, Inceesungvorn B, Bovornratanaraks T. Dynamical stabilization and H-vacancy diffusion kinetics of lightweight complex hydrides: ab initio study for hydrogen storage improvement. Int J Hydrog Energy 2021;46:22591–8. https://doi.org/10.1016/j.ijhydene.2021.04.070.
[95] Evaluation of the Thermodynamic Data of CH3SiCl3 Based on Quantum Chemistry Calculations | Journal of Physical and Chemical Reference Data | AIP Publishing n. d. https://pubs.aip.org/aip/jpr/article-abstract/35/3/1385/242094/Evaluation-of-the-Thermodynamic-Data-of-CH3SiCl3?redirectedFrom=fulltext (accessed April 16, 2025).
[96] Zeng Q, Su K, Zhang L, Xu Y, Cheng L, Yan X. Evaluation of the thermodynamic data of CH3SiCl3 based on quantum chemistry calculations. J Phys Chem Ref Data 2006;35:1385–90. https://doi.org/10.1063/1.2201867.
[97] Lyu J, Elman R, Svyatkin L, Kudiiarov V. Theoretical and experimental research of hydrogen storage properties of Mg and Mg-Al hydrides. J Alloys Compd 2023;938:168618.
[98] Mubashir M, Ali M, Bibi Z, Younis MW, Muzamil M. Efficient hydrogen storage in LiMgF3: a first principle study. Int J Hydrog Energy 2024;50:774–86.